Attitude Estimation Method Using Kalman Filter for MARG Sensors and Its Application

Zeyang Dai

A DISSERTATION

SUBMITTED IN FULFILLMENT OF THE REQUIREMENTS

FOR THE DEGREE OF DOCTOR OF PHILOSOPHY

IN COMPUTER SCIENCE AND ENGINEERING

Graduate Department of Computer and Information Systems

The University of Aizu

2021

The thesis titled

Attitude Estimation Method Using Kalman Filter for MARG Sensors and Its Application

by

Zeyang Dai

is reviewed and approved by:

Chief referee

Professor

Lei Jing Lei Jing 2021-08-12

Professor

Xiang Li Xiang Li

Professor

Kazuyoshi Mori Kazuyoshi Mori

Professor

Keitaro Naruse Keitaro Naru. 2021-08-12

Professor

THE UNIVERSITY OF AIZU

2021

Contents

List of Figures

List of Tables

List of Abbreviations

AHRS	Attitude and heading reference system
CDKF	Central difference Kalman filter
CF	Complementary filter
CKF	Cubature Kalman filter
DCM	Direction cosine matrix
DMA	Direct memory access
eCompass	Electronic compass
EKF	Extended Kalman filter
ENU	East, North, Up coordinates
ESOQ	EStimation of Optimal Quaternion
FCF	Fast complementary filter
FKF	Fast Kalman filter
FOAM	Fast Optimal Attitude Matrix
FOMA	Fast optimal matrix algorithm
FPGA	Field Programmable Gate Arrays
GDA	Gradient descent algorithm
GNA	Gauss newton algorithm
IKF	Indirect Kalman filter
INS	Inertial navigation system
KF	Kalman filter
LEKF	Lightweight Extended Kalman Filter
LMA	Levenberg-Marquadt algorithm
MARG	Magnetic, angular rate and gravity sensor array
MEMS	Micro-electromechanical Systems
MoCap	Motion capture
NED	North, East, Down coordinates
PL	Programmable logic
PS	Processing system
PSD	Power spectral density
QUEST	QUaternion ESTimation
RMSE	Root mean square error
SD card	Secure digital card
SDIO bus	Secure digital input output bus
SPKF	Sigma-point Kalman filter
SVD	Singular Value Decomposition
TCP/IP	Transmission Control Protocol/Internet Protocol
UAV	Unmanned Aerial Vehicle

UKF	Unscented Kalman filter
VFPU	Vector floating point unit
Wi-Fi	Wireless Fidelity

Abstract

Attitude estimation using magnetic, angular rate and gravity (MARG) sensor array is an essential technique for pervasive applications such as controlling of the Unmanned Aerial Vehicle (UAV) and motion capture. These applications employ attitude estimation techniques to obtain the orientation of an object with respect to the Earth's frame. Although an abundance of attitude estimation algorithms has been proposed in the past decades, still there are some challenges, including the trade-off between the accuracy and the computational effort, accelerating of the advanced estimation algorithm, and adapting for the emerging field of motion capture. To deal with them, this thesis addresses these problems in order.

At first, in order to reduce the computational effort and provide a reliable solution for critical constrained resource applications, a quaternion based Lightweight Extended Kalman Filter (LEKF) is proposed. In this filter, we devise a simplified measurement model to process acceleration and magnetic field observations. With this model, on one hand, it need a few computations to process observation vectors. On the other hand, half parameters of Jacobian matrix are constant and others have common factors, this further reduces the computational effort. Moreover, theoretically the accuracy is maintained due to without any linearization of the nonlinear observation model. Experimental results show that the proposed filter provides better performance in terms of either attitude estimation accuracy or computational time.

Further, a matrix operation accelerator is investigated to accelerate the sigma-point Kalman filter (SPKF). Comparing with the typical extended Kalman filter (EKF), SPKF can provide better precision and is more robust, but at the expense of higher computational complexity. On the other hand, the designed accelerator provides a good reusability as well. Experiments are conducted on Zynq-7020, and results indicate that the proposed scheme can reduce about 50% computing time.

Finally, we studied the motion capture system and designed wireless time synchronized motion trackers. Each tracker is composed of a microcontroller enabling Wireless Fidelity (WiFi) connectivity and a MARG sensor array. With built-in WiFi connectivity, it's easily to establish the motion capture system by connecting to a given wireless router, which actually is an scalable asynchronous sensor network. Thus, time synchronization of these trackers is first investigated and an easy-to-operate scheme is proposed, which avoids the complicated hardware design and reduces the cost significantly. What's more, to take full advantage of the performance of the sensors and enable the sensors working at an asynchronous measurement rate, the traditional solution EKF is adapted for multi-rate sensor fusion. Last but not least, several experiments are carried out to validate the feasibility of the proposed motion tracker for motion capture. Experimental results fully prove the reliability of the method for time synchronization and that the proposed motion tracker is feasible for motion capture and there is a good consistency with the optical system.

Chapter 1

Introduction

1.1 Attitude Estimation

Attitude estimation, which is responsible for determining the orientation of the object in three dimensional space, has become the fundamental component in most of modern devices. For example, in controlling of Unmanned Aerial Vehicle (UAV), the correct attitude information are crucial for feedback in the governing control system. In smartphones, attitude information can be utilized for navigation, which has significantly improved user experience in modern daily life. And in gaming industry, active gaming platform is getting more and more popular, where the gaming devices gather the attitude information of users, so as to expand the capability of this style of game, or help open total virtual reality scenarios at the edge of the augmented reality. Attitude estimation of the aforementioned applications is achieved with low-cost magnetic, angular rate and gravity (MARG) sensor array with the recent advances in Micro-electromechanical Systems (MEMS), which normally consists of a 3-axis accelerometer, a 3-axis gyroscope, and a 3-axis magnetometer.

In this section, we provide the knowledge review of attitude estimation using Magnetic, angular rate and gravity sensor array (MARG) sensors. The fundamental concepts are presented in order, including the coordinate system, attitude representations, the MARG sensors model, two fundamental methodologies for extracting attitude information from MARG sensors readings, in which the first is known as Wahba's problem, also termed as deterministic attitude estimation of the accelerometer and magnetometer, and the second is about the attitude kinematics which obtains the attitude through integrating the gyroscope measurements. Then, the concept of dynamic filtering and estimation is introduced, which is actually the sensor fusion technique, and aims at eliminating the bottleneck of single sensor. Last but not least, issues in practical applications are discussed.

1.1.1 Coordinate systems

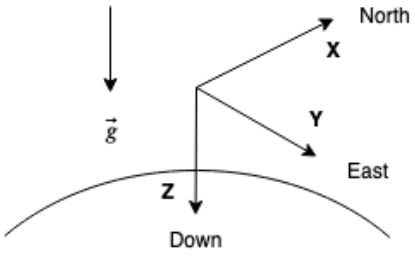

Figure 1.1: NED Coordinates

For Attitude and heading reference system or local tangent plane coordinates, there are two well-known coordinate systems; East, North, Up coordinates (ENU) and North, East, Down coordinates (NED). The former is used in geography, while the later one is specially used in aerospace. The local ENU coordinates are formed from a plane tangent to the Earth's surface fixed to a specific location and the east axis is labeled as x, the north y and the up z by convention, while for NED coordinates the north axis is labeled as x, the east y and the down z. It is easy to find that, ENU coordinates and NED coordinates are similar except for swapping 'down' for 'up' and x for y. In this paper, like most of other researchers, NED coordinate system is chosen as the benchmark and implemented for all the designed applications in this thesis, as defined in Fig. 1.1.

1.1.2 Attitude representation

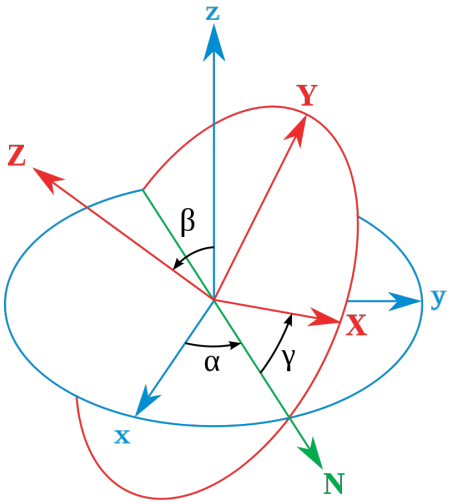

Figure 1.2: Rotation with Respect to a Fixed Coordinate

With respect to a reference frame, we have three frequently used ways to describe the orientation of a rigid body, they are the equivalent form and include the Euler angles, Direction cosine matrix (DCM) and quaternion respectively. In the following, we will

discuss the three representations separately and describe the transformational relation between them. The Euler angles are three angles introduced by Leonhard Euler, in general they are termed as roll, pitch and yaw, and denoted as ϕ, θ and ψ or α, β and γ in mathematical. According to Euler's rotation theorem, the three angles can be used to describe any rotation, as shown in Fig. 1.2 where ϕ is the angle between the x axis and the N axis, θ for the angle between the z axis and the Z axis and ψ for the angle between the N axis and the X axis. We assume the rotation is in x-convention. When writing the rotation in terms of rotation matrices, the rotation is defined to be

$$R(\phi, \theta, \psi) = R(\psi)R(\theta)R(\phi) \tag{1.1}$$

where

$$R(\psi) = \begin{pmatrix} cos(\psi) & sin(\psi) & 0 \\ -sin(\psi) & cos(\psi) & 0 \\ 0 & 0 & 1 \end{pmatrix} \tag{1.2}$$

$$R(\theta) = \begin{pmatrix} 1 & 0 & 0 \\ 0 & cos(\theta) & sin(\theta) \\ 0 & -sin(\theta) & cos(\theta) \end{pmatrix} \tag{1.3}$$

$$R(\phi) = \begin{pmatrix} cos(\phi) & sin(\phi) & 0 \\ -sin(\phi) & cos(\phi) & 0 \\ 0 & 0 & 1 \end{pmatrix} \tag{1.4}$$

Henceforth, the final equation can be rewritten as

$$R(\phi, \theta, \psi) = \begin{pmatrix} r_{11} & r_{12} & r_{13} \\ r_{21} & r_{22} & r_{23} \\ r_{31} & r_{32} & r_{33} \end{pmatrix} \tag{1.5}$$

where

$$\begin{aligned} r_{11} &= cos(\psi)cos(\phi) - cos(\theta)sin(\phi)sin(\psi) \\ r_{12} &= cos(\psi)sin(\phi) + \cos(\theta)cos(\phi)sin(\psi) \\ r_{13} &= sin(\psi)sin(\theta) \\ r_{21} &= -sin(\psi)cos(\phi) - cos(\theta)sin(\phi)cos(\psi) \\ r_{22} &= -sin()sin(\phi) + cos(\theta)cos(\phi)cos(\psi) \\ r_{23} &= cos(\psi)sin(\theta) \\ r_{31} &= sin(\theta)sin(\phi) \\ r_{32} &= -sin(\theta)cos(\phi) \\ r_{33} &= cos(\theta) \end{aligned} \tag{1.6}$$

The derived matrix is the so-called DCM. Let $\omega = \begin{bmatrix} \omega_x & \omega_y & \omega_z \end{bmatrix}$ be the angular velocity on axis x, y and z respectively of the rigid body expressed in the body frame B, then, the rigid body kinematics equation is given by

$$\dot{R} = RS(\omega) \tag{1.7}$$

where $S(\omega)$ is the skew symmetric matrix and given by

$$S(\omega) = \begin{pmatrix} 0 & -\omega_z & \omega_y \\ \omega_z & 0 & -\omega_x \\ -\omega_y & \omega_x & 0 \end{pmatrix} \tag{1.8}$$

For the rotation from the sensor frame to the body frame, the kinematics is expressed

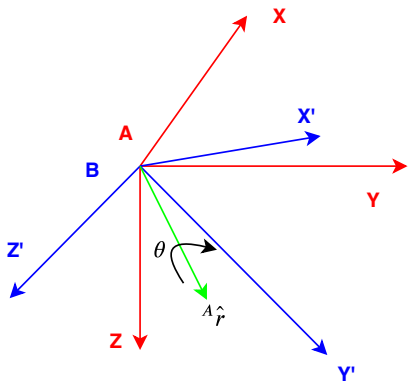

Figure 1.3: Rotation from Frame A to Frame B, of Angle θ Around the Axis ${}^{A}\hat{r}$

as

$$\dot{R} = -S(\omega)R \tag{1.9}$$

A quaternion, introduced in [2–4], is a four dimensional complex number and can be used to represent arbitrary orientation as well. For example, in Fig. 1.3, any orientation of frame B relative to frame A can be achieved through a rotation of angle θ around an axis ${}^{A}\hat{r}$ defined in frame A, we employ the quaternion ${}^{B}_{A}\mathbf{q}$ to express the rotation, which is defined by

$$\begin{aligned} {}^{B}_{A}\mathbf{q} &= \begin{bmatrix} w & x & y & z \end{bmatrix} \\ &= \begin{bmatrix} q_0 & q_1 & q_2 & q_3 \end{bmatrix} \\ &= \begin{bmatrix} cos(\frac{\theta}{2}) & -r_x sin(\frac{\theta}{2}) & -r_y sin(\frac{\theta}{2}) & -r_z sin(\frac{\theta}{2}) \end{bmatrix} \end{aligned} \tag{1.10}$$

where r_x, r_y and r_z are the components of the units vector ${}^{A}\hat{r}$ in x, y and z axes of frame A respectively, while the elements, w, x, y, z and q_0, q_1, q_2 q_3, are the frequently-used different equivalent forms of the quaternion definition. Conventionally, all the

quaternions are an unit length, this is to say, the quaternion is subject to

$$\|\mathbf{q}\|^2 = q_0^2 + q_1^2 + q_2^2 + q_3^2 = 1 \tag{1.11}$$

With the quaternion of unit length, the frequently used quaternion arithmetic is defined as the following. The conjugate of the quaternion is

$${}^B_A\mathbf{q}^* = {}^A_B\mathbf{q} = \begin{bmatrix} q_0 & -q_1, -q_2, & -q_3 \end{bmatrix} \tag{1.12}$$

where $*$ denotes the conjugate of the quaternion. The quaternion product of two quaternions, $\mathbf{a}$ and $\mathbf{b}$, is defined by

$$\begin{aligned} \mathbf{a} \otimes \mathbf{b} &= \begin{bmatrix} a_0 & a_1 & a_2 & a_3 \end{bmatrix} \otimes \begin{bmatrix} b_0 & b_1 & b_2 & b_3 \end{bmatrix} \\ &= \begin{bmatrix} a_0b_0 - a_1b_1 - a_2b_2 - a_3b_3 \\ a_0b_1 + a_1b_0 + a_2b_3 - a_3b_2 \\ a_0b_2 - a_1b_3 + a_2b_0 + a_3b_1 \\ a_0b_3 + a_1b_2 - a_2b_1 + a_3b_0 \end{bmatrix}^T \end{aligned} \tag{1.13}$$

where $\otimes$ denotes the Hamilton product. Note that the quaternion product is not commutative, that is, $\mathbf{a} \otimes \mathbf{b} \neq \mathbf{b} \otimes \mathbf{a}$. With another quaternion ${}^C_B\mathbf{q}$ to express the rotation from frame B to frame C, the compounded orientation ${}^C_A\mathbf{q}$ can be obtained by

$${}^C_A\mathbf{q} = {}^B_A\mathbf{q} \otimes {}^C_B\mathbf{q} \tag{1.14}$$

For the rotation between two same vectors, ${}^Av$ and ${}^Bv$, which are described in frame A and frame B respectively, we insert 0 to each vector as the first element and figure out the rotation by

$${}^Bv = {}^B_A\mathbf{q} \otimes {}^Av \otimes {}^B_A\mathbf{q}^* \tag{1.15}$$

As mentioned before, these representation are equivalent. The orientation ${}^B_A\mathbf{q}$ also can be represented as the rotation matrix defined by

$$R({}^B_A\mathbf{q}) = \begin{bmatrix} 2q_0^2 - 1 + 2q_1^2 & 2(q_1q_2 + q_0q_3) & 2(q_1q_3 - q_0q_2) \\ 2(q_1q_2 - q_0q_3) & 2q_0^2 - 1 + 2q_2^2 & 2(q_2q_3 + q_0q_1) \\ 2(q_1q_3 + q_0q_2) & 2(q_2q_3 - q_0q_1) & 2q_0^2 - 1 + 2q_3^2 \end{bmatrix} \tag{1.16}$$

where the conversion is a homogeneous expression. The reverse mapping, from the rotation matrix to the quaternion, though the Shepperds's method [5] is usually considered

as the solution, the revised framework [6] is recommended and defined by

$$q_0 = \frac{1}{2}\begin{cases} t_0 & \text{if } r_{22} > -r_{33}, r_{11} < -r_{22}, r_{11} > -r_{33} \\ (r_{23} - r_{32})/t_0 & \text{if } r_{22} < -r_{33}, r_{11} > r_{22}, r_{11} > r_{33} \\ (r_{31} - r_{13})/t_0 & \text{if } r_{22} > r_{33}, r_{11} < -r_{22}, r_{11} < -r_{33} \\ (r_{12} - r_{21})/t_0 & \text{if } r_{22} < r_{33}, r_{11} < -r_{22}, r_{11} < r_{33} \end{cases} \tag{1.17}$$

where $t_0 = \sqrt{1 + r_{11} + r_{22} + r_{33}}$,

$$q_1 = \frac{1}{2}\begin{cases} (r_{23} - r_{32})/t_1 & \text{if } r_{22} < -r_{33}, r_{11} > r_{22}, r_{11} > r_{33} \\ t_1 & \text{if } r_{22} > -r_{33}, r_{11} < -r_{22}, r_{11} > -r_{33} \\ (r_{12} + r_{21})/t_1 & \text{if } r_{22} > r_{33}, r_{11} < -r_{22}, r_{11} < -r_{33} \\ (r_{31} + r_{13})/t_1 & \text{if } r_{22} < r_{33}, r_{11} < -r_{22}, r_{11} < r_{33} \end{cases} \tag{1.18}$$

where $t_1 = \sqrt{1 + r_{11} - r_{22} - r_{33}}$,

$$q_2 = \frac{1}{2}\begin{cases} (r_{31} - r_{13})/t_2 & \text{if } r_{22} < -r_{33}, r_{11} > r_{22}, r_{11} > r_{33} \\ (r_{12} + r_{21})/t_2 & \text{if } r_{22} > -r_{33}, r_{11} < -r_{22}, r_{11} > -r_{33} \\ t_2 & \text{if } r_{22} > r_{33}, r_{11} < -r_{22}, r_{11} < -r_{33} \\ (r_{23} + r_{32})/t_2 & \text{if } r_{22} < r_{33}, r_{11} < -r_{22}, r_{11} < r_{33} \end{cases} \tag{1.19}$$

where $t_2 = \sqrt{1 - r_{11} + r_{22} - r_{33}}$,

$$q_3 = \frac{1}{2}\begin{cases} (r_{12} - r_{21})/t_3 & \text{if } r_{22} < -r_{33}, r_{11} > r_{22}, r_{11} > r_{33} \\ (r_{31} + r_{13})/t_3 & \text{if } r_{22} > -r_{33}, r_{11} < -r_{22}, r_{11} > -r_{33} \\ (r_{23} + r_{32})/t_3 & \text{if } r_{22} > r_{33}, r_{11} < -r_{22}, r_{11} < -r_{33} \\ t_3 & \text{if } r_{22} < r_{33}, r_{11} < -r_{22}, r_{11} < r_{33} \end{cases} \tag{1.20}$$

where $t_3 = \sqrt{1 - r_{11} - r_{22} + r_{33}}$. This is the revised version and more accurate and stable. The Euler angles can be extracted from ${}^{B}_{A}\mathbf{q}$ by

$$\begin{aligned} \psi &= atan2(2q_1q_2 - 2q_0q_3, 2q_0^2 + 2q_2^2 - 1) \\ \theta &= -asin(2q_1q_3 + 2q_0q_2) \\ \phi &= atan2(2q_2q_3 - 2q_0q_1, 2q_0^2 + 2q_3^2 - 1) \end{aligned} \tag{1.21}$$

where $atan2$ and $asin$ are inverse the trigonometric functions.

1.1.3 MARG sensors model

As mentioned above, each MARG sensor is composed of a 3-axis MEMS angular rate gyro traid, a 3-axis MEMS accelerometer, and a 3-axis magnetometer. Regardless of which sensor of them, there are many kinds of noise when in use, which include such as the scale factor, misalignment, and bias. In order to mathematically correct these errors, the sensor model is required so that we can conduct analysis.

For modern MARG sensors, the main sources of the sensor error include bias, scale factor and non-orthogonality, henceforth, an unified sensor model [7] is used in this paper, that is

$$y_k = S_k T_k u_k - b_k + n_k \tag{1.22}$$

where k represents the sensor type, u_k is the truth physical quantities in metric unit, and y_k is the sensor reads. S_k is the scale factor. T_k is the Gram–Schmidt orthogonalization matrix for compensating the error of non-orthogonality. b_k is the bias vector, normally it's the constant. n_k is the vector of white noise caused by thermo-mechanical events and stated as a zero mean process with a standard deviation equal to σ_k. For the 3-axis sensor, y_k, u_k, b_k and n_k is 3×1 vectors, while S_k and T_k are 3×3 matrices. Although the sources of error are almost same, they have different contributions to the overall orientation accuracy for different sensors, we discuss them separately in the following.

A gyroscope is the sensor that measures the angular rate, the orientation for which is obtained by integrating the measured angular rate over time. Evidently, constant bias errors grow linearly with time and the bias has a significant effect on the accuracy of the orientation. But not to worry, we can find the constant bias error of a gyro by taking the average of the output over a long period of time while the device is not rotating, and subtract it from subsequent measurements to eliminate this form of error. In contrast, white noise has no effect on the integrated orientation due to it is a zero mean process. Besides, the bias stability, not represented in the sensor model, generally it is very small and not necessary to concern for the low-cost MARG, is the another often concerned noise resource and tell us how stable the bias of a gyroscope is over a certain specified period of time.

An accelerometer is responsible for measuring the acceleration. In modern devices, the bias of the accelerometer is very small and has a minimal effect on the accuracy of the orientation.

An magnetometer measures the strength and direction of the local magnetic field. Different with the gyroscope and the accelerometer, the main sources of error are the soft iron and hard iron due to its measurements are subjected to distortion. Soft iron distortions are considered deflections or alterations in the existing magnetic field and commonly caused by metals such as nickel and iron, while hard iron distortion caused by the magnetic material or magnetized objects will cause a permanent bias in the sensor

output. In actual use, the magnetometer is required to do the ellipse fitting to compensate such two error for a given application scenario.

1.1.4 Wahba's problem

Wahba's problem [8], also known as static attitude determination, involves numerically determining the attitude taking advantage of the body vector observations without considering its kinematics. For instance, the attitude determination using the measurements of accelerometer and magnetometer. In this problem, simultaneously two sets of N observed unit vectors $V_1, ..., V_N$ and $W_1, ..., W_N$ are respectively known in the reference coordinate system and the body frame, the attitude is merely regarded as a matrix that transforms the reference vectors $V_1, ..., V_N$ in the reference frame to the vectors $V_1, ..., V_N$ in the body frame and as a result, can be obtained by mathematical optimization techniques. In this way, the rotation matrix, orthogonal matrix R, is numerically found by minimizing

$$L(R) = \frac{1}{2}\sum_{i=1}^{N} a_i |W_i - RV_i|^2 \tag{1.23}$$

where the a_i are non-negative weights. By normalizing the weights, that is, $\sum_{i=1}^{N} a_i = 1$, the loss function is rewritten in the straightforward form

$$L(R) = 1 - \sum_{i=1}^{N} a_i W_i^T R V_i = 1 - tr(RB^T) \tag{1.24}$$

where tr denotes the trace of the matrix and B is defined as

$$B = \sum_{i=1}^{N} a_i W_i V_i^T \tag{1.25}$$

This equation converts the problem to maximum the term $tr(RB^T)$ by finding the appropriate R and attitude is found on an optimization basis. The found attitude normally comes with a lower accuracy due to the discarding of the information of the system dynamics.

Solutions to the Wahba's least squares problem includes the earliest attitude reconstruction method TRAID [9], Singular Value Decomposition (SVD) method [8], Fast Optimal Attitude Matrix (FOAM) [10], Q-Method [11], QUaternion ESTimation (QUEST) [12], EStimation of Optimal Quaternion (ESOQ) [13–15], the recent consideration [16] and so on. For more details of this problem readers are referred to [17].

1.1.5 Attitude kinematics

As discussed before, gyroscope measures the angular rate of the rigid body in the sensor frame. With an known initial condition, the attitude can be obtained by integrating the readings of gyroscope over time. In this way, we have to derive the attitude kinematics, which relates the attitude at time step k to the attitude at step $k+1$. Substituting the formula 1.9 and representing in quaternion,

$$\dot{\mathbf{q}} = \frac{1}{2}[\mathbf{\Omega}\times]\mathbf{q} \tag{1.26}$$

where

$$[\mathbf{\Omega}\times] = \begin{pmatrix} 0 & -\omega_x & -\omega_y & -\omega_z \\ \omega_x & 0 & \omega_z & -\omega_y \\ \omega_y & -\omega_z & 0 & \omega_x \\ \omega_z & \omega_y & -\omega_x & 0 \end{pmatrix} \tag{1.27}$$

Then integrating over time is

$$\mathbf{q}_{k+1} = \left\{ \mathbf{I}_{4\times 4} + \frac{1}{2}[\mathbf{\Omega}\times] \right\} \mathbf{q}_k \tag{1.28}$$

where k denotes the time step, while $\mathbf{I}_{4\times 4}$ is the 4×4 identity matrix. The state transition formula takes the full system dynamics into account. However, when there are bias errors that occurs in the gyroscope readings, this iterative formula would lead to the significant accumulative error of the estimated angles with the increasing of time. As so, we generally fuse the measurements of the gyroscope and observations from the accelerometer and magnetometer together as the reliable solution, this is also called the sensor fusion techniques and leads us to the next topic.

1.1.6 Dynamic filtering and estimation

Dynamic filtering and estimation is the sensor fusion technique that aims at eliminating the bottleneck of each sensor, and generally called attitude estimation algorithms. In the past decades, there are amounts of attitude estimation algorithms that have been developed. Theses algorithms can be divided into two categories roughly; the Complementary filter (CF) and Kalman filter (KF) based methods. Comparing with KF based methods, CF based methods obtain the accurate attitude by compensating for each other in the frequency domain and have more efficient computations. Early thoughts of CF based methods are raised around 1990 by Foxlin who first applied MARG sensors to monitor the attitude motion of human's head [18]. In recent, Madgwick computed the attitude using Gradient descent algorithm (GDA) via the quaternion representation in [19]. Particularly Wu proposed faster and more robust Fast complementary filter

(FCF) than before. However, the typical drawback of CF is that the gain is constant and always empirically given for one time and the inability to adapt the weight for another quite different scenario, still can not be overcome completely. In contrast, KF based methods are always taken as the common solution due to its guaranteed performance. Therefore, this thesis mainly involves the theory of KF.

The KF is by far the most common one and statistically the optimal estimate for linear system with independent white Gaussian noises. Especially only one iteration is required for KF applications since the rate of convergence is higher than the angular speed in general. As a result of the guaranteed high performance, amounts of KF based methods have been developed. In particular to adapt for nonlinear systems, such methods like Extended Kalman filter (EKF) and the advanced SPKF, which includes Unscented Kalman filter (UKF) [20], Central difference Kalman filter (CDKF) [21, 22] and Cubature Kalman filter (CKF) [23], are developed in the later. For more discussion, the introduction of KF is given in the Chapter 2, and the presentation and acceleration of SPKF is explained in the Chapter 4.

1.1.7 Issues in practical applications

In recent, attitude estimation using MARG sensors becomes one of the promising frontiers. On one hand, it has the characteristics of good wearability and low-cost. On the other hand, it provides acceptable performance and not subject to the sites during application. However, we are still facing challenges, and would like to discuss the following three issues:

- For low-end devices, the resource are limited strictly, thus finding the lightweight solution is absolutely imperative.
- For advanced Kalman filters based applications, how to achieve the performance of being real-time has to be considered.
- In the real application of motion capture, where the distributed sensor nodes obtain the orientation information of the object so as to reconstruct the motion trajectory, as a result, time synchronization between the distributed sensor nodes needs to be investigated. Besides, due to the sensors of the accelerometer, the gyroscope, and the magnetometer works in an asynchronous measurement rate, multi-rate sensor fusion also should be concerned.

1.2 Thesis Organization

The structure of this dissertation and the relationship of three main chapters are illustrated in Fig. 1.4. This dissertation is organized in the following manner.

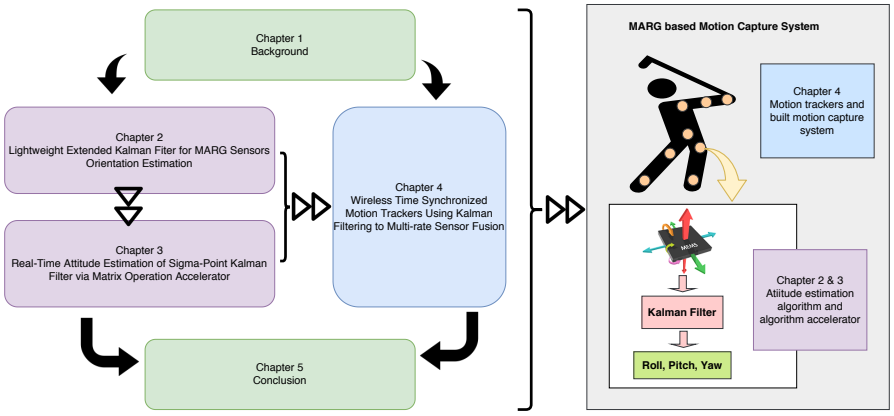

Figure 1.4: Thesis Structure and the Relationship of Three Main Chapters

First of all, research background is introduced in Chapter 1, which mainly introduce the fundamental conceptions of attitude estimation such as coordinate systems, attitude representations and so on. In addition, the thesis organization and the main contributions are also explained in this chapter. Secondly, the related work is described in Chapter 2. In order to reduce the computational effort, Chapter 3 describes a novel Lightweight Extended Kalman Filter (LEKF) and the details of filter design is presented, particular the simplified measurement model is derived. For the experiment, the proposed filter is evaluated from two aspects; the accuracy of attitude estimation for different application scenario and the computing cost. Further, aiming at accelerating the advanced KF, namely SPKF, a matrix operation accelerator executing on Field Programmable Gate Arrays (FPGA) is designed as the solution in Chapter 4. This accelerator guarantees the good reusability and is assessed on Zynq-7020. Considering the time synchronization in an asynchronous sensor network, in Chapter 5, we study the motion capture system and propose a novel wireless time synchronized motion trackers. We first introduce the work principles of the trackers, including the scheme of time synchronization. Then the KF to multi-rate sensor fusion is explained, which enables the sensor working at an asynchronous measurement rate and takes full advantage of the performance of the sensors. The experiments of time synchronization assessment, the accuracy evaluation of attitude estimation, the motion tracking during human walking are conducted to validate the feasibility of the proposed motion tracker. At last, Chapter 6 gives the concluding remarks of this dissertation.

1.3 Contributions

This dissertation is a report about three years of my research on the topics of motion capture theory and application using KF for MARG sensor array. We start the research from two ways; one is the attitude estimation theory; two is the investigation of the motion capture system using MARG sensor array. The results are described in Chapter

3, 4 and 5. The main contributions of each chapter are summarized as follows.

(1) **Chapter 3. Lightweight extended Kalman filter for MARG sensors orientation estimation**

In modern devices, most of devices is equipped with a navigation system that involves the attitude estimation using inertial sensors, and power consumption has become the significant evaluation metrics for better cruising ability, in which the resource is strictly limited. As a result, this arise a key problem of seeking a low power consumption and accurate algorithm for attitude estimation. To address such problem, this chapter,

- A simplified measurement model is derived from TRAID method. As a result of the simplified measurement model, up to half of parameters of Jacobian matrix are constant and only a few amount of computation is required for other parameters of Jacobian, which are similar and have the common factors.
- A quaternion-based LEKF is constructed with the structure of EKF.
- The accuracy of the proposed filter for the drone application and human motion capture is evaluated with the golden truth provided by the optical system, namely Vicon.
- The computational cost is evaluated with comparison to two existing algorithms; Indirect Kalman filter (IKF) and Fast Kalman filter (FKF).

(2) **Chapter 4. Real-time attitude estimation of sigma-point Kalman filter via matrix operation accelerator**

With the increasing demands for the accuracy and robustness, SPKF is becoming the promising solution. However, the higher accuracy and robustness are at the cost of higher computational efforts. To deal with this, this chapter,

- The general structure of SPKF is summarized and the attitude estimation filter based on SPKF is designed.
- The matrix operation accelerator is proposed on FPGA. This accelerator significantly improved the re-usability for matrix operation based algorithm and succeeds in accelerating SPKF.
- Evaluation of the performance of the designed accelerator is conducted on Zynq-7020 from two aspects; performance of the proposed accelerator and the speedup ratio for SPKF.

(3) **Chapter 4. Wireless time synchronized motion trackers using kalman filtering to multi-rate sensor fusion**

For existing MARG sensor array based capture systems, time synchronization between trackers is normally ignored. Although some commercial devices such [24] provide accurate hardware solution, the hardware solution usually raise the cost significantly and exceed the actual needs of the precision. therefore, in this paper,

- Wireless time synchronized motion trackers are presented. Time synchronization for built motion capture system using the designed trackers are solved by the consistency of the gyroscopes under the same condition. This method is actually a software-based method and cost saving.
- A quaternion-based KF to multi-rate sensor fusion is proposed, which enables the sensor working at an synchronous measurement rate and takes full advantage of the performance of the sensors.
- To verify the feasibility of the proposed motion trackers for motion tracking, firstly time synchronization is assessed, then the accuracy of the attitude estimation is evaluated with the reference measurements provided by Vicon, at the last the built motion capture system is validated during human walking and the results are compared with results extracted from the optical system.

1.4 Publications

The following papers have been published or submitted to major journals and conference.

(1) **Major journal paper**

1. **Zeyang Dai**, and Lei Jing. Lightweight Extended Kalman Filter for MARG Sensors Attitude Estimation. IEEE Sensors Journal, 2021.
   DOI: 10.1109/JSEN.2021.3072887.
2. Linjun Zhao, Chuanhua Su, **Zeyang Dai**, Huakun Huang, Shuxue Ding, Xinyi Huang and Zhaoyang Han. (2019). Indoor device-free passive localization with DCNN for location-based services. The Journal of Supercomputing, 1-18.
   DOI: 10.1007/s11227-019-03110-2.

(2) **Major conference paper**

1. **Zeyang Dai**, and Lei Jing. Real-Time Attitude Estimation of Sigma-Point Kalman Filter via Matrix Operation Accelerator. 2019 IEEE 13th International Symposium on Embedded Multicore/Many-core Systems-on-Chip (MCSoC), Singapore, Singapore, 2019, pp. 342-346.
   DOI: 10.1109/MCSoC.2019.00055.

2. **Zeyang Dai**, Chenghong Lu and Lei Jing. Time Drift Compensation Method on Multiple Wireless Motion Capture Nodes. In 2020 13th International Conference on Human System Interaction (HSI) (pp. 266-271). IEEE.
   DOI: 10.1109/HSI49210.2020.9142648.

3. Lei Jing, **Zeyang Dai** and Yiming Zhou. Wearable Handwriting Recognition with an Inertial Sensor on a Finger Nail. 2017 14th IAPR International Conference on Document Analysis and Recognition (ICDAR), Kyoto, 2017, pp. 1330-1337.
   DOI: 10.1109/ICDAR.2017.219.

4. Yiming Zhou, **Zeyang Dai** and Lei Jing. A Controlled Experiment Between Two Methods on Ten-Digits Air Writing. 2016 IEEE International Conference on Computer and Information Technology (CIT), Nadi, 2016, pp. 299-302.
   DOI: 10.1109/CIT.2016.112.

Chapter 2

Related Work

In this section, two related works are described; first to introduce the basic theory of KF, and second to introduce the method of noise identification for MARG sensors.

2.1 Kalman Filter

KF actually is a recursive solution to the discrete-data linear filtering problem and was proposed in [25] in 1960 by R.E. Kalman. To date, there are many materials that can be found to friendly introduce the general idea of KF, such as [26–28]. This section will briefly introduce the theory of KF.

KF addresses the general problem of estimating the state $x_k \in \mathcal{R}^n$ of a linear discrete-time system, which is governed by the linear process model and the measurement model, that is

$$\begin{aligned} x_k &= A_k x_{k-1} + B\mu_k + \omega_k \\ z_k &= H_k x_k + \upsilon_k \end{aligned} \tag{2.1}$$

where the $n \times n$ matrix A_k relates the state at the time step $k-1$ to the next state at step k, the $n \times l$ matrix B is the control input model which is applied to the $l \times n$ control vector μ_k, while the $m \times n$ matrix H_k is the observation model and the $m \times n$ vector z_k is the observation the the true state x_k. The $n \times n$ vector ω_k and $m \times n$ vector υ_k are the process noise and measurement noise respectively, and they are assumed to be independent and obey the Gaussian distribution with covariance Q and R respectively, as the following probability distributions indicated

$$\begin{aligned} p(\omega) &\sim N(0, Q) \\ p(\upsilon) &\sim N(0, R) \end{aligned} \tag{2.2}$$

With the symbol $\hat{x_k^-} \in \mathcal{R}^n$ to express the $a\ priori$ state estimate at step k, and $\hat{x_k} \in \mathcal{R}^n$ to express the $a\ posteriori$ state estimate at step k, the $a\ priori$ and $a\ posteriori$ errors

can be defined to be

$$\begin{aligned} e_k^- &= x_k - \hat{x}_k^- \\ e_k &= x_k - \hat{x}_k \end{aligned} \tag{2.3}$$

Then the $a\ priori$ estimate error covariance is

$$P_k^- = E\left[e_k^- e_k^{-T}\right] \tag{2.4}$$

and the $a\ posteriori$ estimate error covariance is

$$P_k = E\left[e_k e_k^T\right] \tag{2.5}$$

Considering

$$\hat{x}_k = \hat{x}_k^- + K_k(z_k - H_k\hat{x}_k^-) \tag{2.6}$$

where this formula is to compute an $a\ posteriori$ state estimate $\hat{x}_k$ as a linear combination of an $a\ priori$ estimate $\hat{x}_k^-$ and a weighted difference between an actual measurement z_k and a measurement prediction $H_k\hat{x}_k^-$, and the difference $(z_k - H_k\hat{x}_k^-)$ is called the measurement $innovation$ or the $residual$. The $n \times m$ matrix K is the gain for minimizing the $a\ posteriori$ error covariance. Substituting the above equations, the resulting K is given by

$$K_k = P_k^- H_k^T (H_k P_k^- H_k^T + R_k)^{-1} \tag{2.7}$$

Then we will get the well-known KF formulas and the summarized structure is graphically presented in Fig. 2.1.

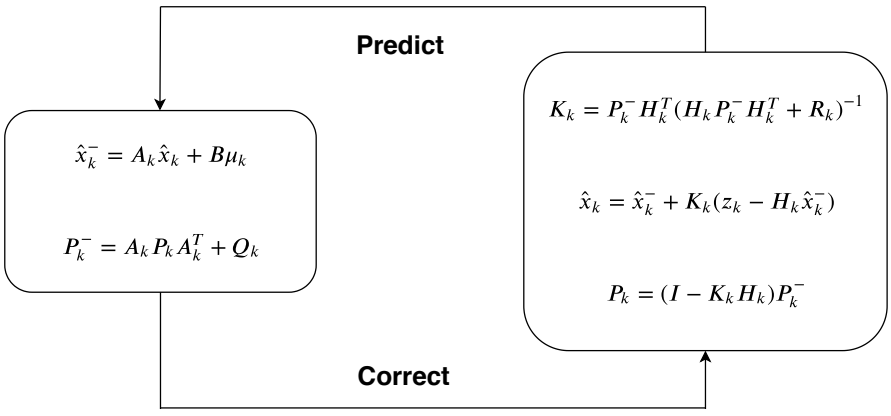

Figure 2.1: Structure of Kalman Filter

As described above, KF is to deal with the problem of estimating the state $x_k \in \mathcal{R}^n$ of a linear discrete-time system, when the process model or the measurement model is

non linear, that is,

$$\begin{aligned} x_k &= f(x_{k-1}, \mu_k) + W\omega_k \\ z_k &= h(x_k) + V\upsilon_k \end{aligned} \tag{2.8}$$

This problem is solved by the well-known EKF [29,30], which linearizes the estimation around the current estimate using the partial derivatives of the process and measurement functions to compute estimates. Actually this method is akin to a Taylor series. The structure of EKF is exactly same with KF, the only thing we have to do is figure out the state transition matrix A_k, observation matrix H_k, the Jacobian matrix of partial derivatives of $f(x_{k-1}$ with respect to ω, the Jacobian matrix of partial derivatives of $h(x_k)$ with respect to υ, they are defined by

$$A_k = \frac{\partial f}{\partial x}\Big|_{\hat{x}_{k-1}}, \quad H_k = \frac{\partial h}{\partial x}\Big|_{\hat{x}_k^-} \tag{2.9}$$

and

$$W = \frac{\partial f}{\partial \omega}\Big|_{\hat{x}_{k-1}}, \quad V = \frac{\partial h}{\partial \upsilon}\Big|_{\hat{x}_k^-} \tag{2.10}$$

As for other advanced KFs, which aims at compensating the errors caused by the large linearity of the system, are not introduced here.

2.2 Noise Identification

When designing the KF, the configuration using correct noise characteristics is conductive to achieve the optimal performance of KF. Although the noise characteristics of the sensor are specified in the corresponding product datasheet, it is necessary to learn how to identify the noise. On one hand, sometime the specified parameters are not practical for low-cost devices. On the other hand, understanding the noise identification is beneficial for us to tune the parameters of KF.

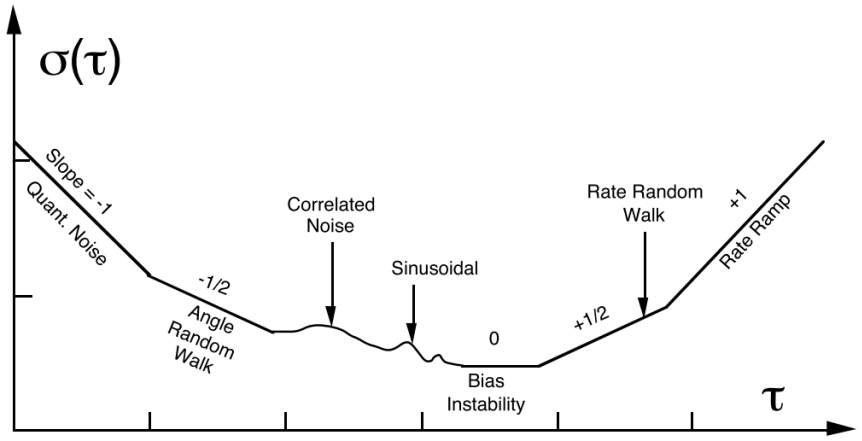

Figure 2.2: Sample Plot of Square-Root Allan Variance Analysis Results [1]

For MARG sensors, there are five basic noise terms [31], they are quantization noise, the most concerned **angle random walk**, bias instability, rate random walk, and rate ramp. For estimation of MARG sensors' stochastic errors, several methods have been devised, that is, adaptive Kalman filtering, Power spectral density (PSD), auto-correlation function and Allan variance [32]. Among them, Allan variance [1, 33, 34] is the simplest one, which is a method of representing the root mean square random-drift errors as a function of averaging times. Assume that we have N measurements $y = \{y_1, y_2, ..., y_N\}$ with sample time τ_0. The cluster time with length m is expressed as $\tau_m = m\tau_0$. Thus, Allan variance is expressed as

$$\sigma_y^2\tau = \frac{1}{2(M-1)} \sum_{j=1}^{M-1} \left[\overline{y}_{j+1} - y_j\right]^2 \tag{2.11}$$

where M denotes the number of cluster samples $\overline{y}_k$, and the average of cluster is defined by

$$\overline{y}_k(m) = \frac{1}{m} \sum_{i=1}^{m} y_{m(k-1)+i} \quad 0 \leq k \leq M \tag{2.12}$$

where k indicates the k_{th} cluster and the cluster time m is subject to $m \leq N/2$. Then we plot square-root of the results in log-log plot, it should look like the one shown in Fig. 2.2. Different terms appear in different regions of τ. This allows us to identify various random that exist in the measurements processes easily.

Chapter 3

Lightweight Extended Kalman Filter for MARG Sensors Attitude Estimation

3.1 Introduction

MARG sensors have been widely applied to our surrounding devices. These applications include the UAV [35, 36], human motion capture [37], wearable devices [38], and so on. The MARG sensors are employed to compute the orientation of a rigid body with respect to an inertial frame so as to precisely control the actuators or extract motion features. Normally, orientation parameters can be acquired from two approaches. The first approach, related to the Inertial navigation system (INS), is to do integral of angular rates from gyroscope over time if initial conditions are known. The second approach is summarized as Wahba's problem [8, 17] formed by at least two vector observations. As is known, in the case of low-cost MARG sensors, gyroscope measures the angular velocity of a moving object. Accelerometer and magnetometer measure the earth's gravitational and magnetic fields respectively to provide an absolute reference of orientation with the assumption that the measurements are not disturbed by any external noises. Their performance are always subject to their inherent drawbacks, for example, drift error, external disturbance, and so on, that means we can not just rely on any one to obtain accurate orientation estimation. For instance, the angular-rate integral will diverge very fast as time goes, and accelerometer's output will be disturbed by non-gravitational acceleration when the motion isn't flat. There are too many uncertainties inside almost every process of their sensing. Hence, a reliable attitude estimation solution is to fuse them together using sensor fusion techniques.

Looking back on the past decades, amounts of approaches have been proposed for sensor fusion. Roughly, we can classify them into two categories: complementary fil-

ter [39–41] and Kalman filter [42–44] based methods. Complementary filters obtain a more accurate orientation estimation by compensating for each sensor in the frequency domain, while Kalman filters adopt a probabilistic determination of the state modeled as a Gaussian distribution given the system model. Early thoughts of complementary filter based solutions are raised around 1990 by Foxlin who first applied MARG sensors to monitor the attitude motion of human's head [18], the strategy of which is that combines the accelerometer and magnetometer as the Electronic compass (eCompass) [45], the problem of which can be effectively solved by optimization algorithms like GDA [39], Gauss newton algorithm (GNA) [46] and Levenberg-Marquadt algorithm (LMA) [47] or solutions to Wahba's problem for example TRIAD [48, 49], Fast optimal matrix algorithm (FOMA) [10], QUEST [50] and ESOQ [13]. Based on this, Mahony in 2008 studied the attitude representation on spectial orthogonal groups by different way [51]. Madgwick computed the attitude using the GDA via quaternion representation [39]. Especially FCF [40] proposed by Wu was proved to be faster and more robust than previous. Although all the above solutions are the constant gain complementary filters, the typical drawback of which is that the gain is always empirically given for one time and the inability to adapt the weight for another quite different scenario when their accuracy is affected, it has reflected the development trend where lightweight solutions with maintained accuracy are preferred when seeking the balance between the performance and the computation complexity.

The Kalman filter is by far the most common one and statistically the optimal estimator for linear system with independent white Gaussian noises, generally one iteration is sufficient for convergence. As a result of the excellent performance, considering that the systems are normally nonlinear, and to apply Kalman filter to nonlinear systems, adaption and implementation of Kalman filter for nonlinear systems are significantly investigated in the past decades. Adapted methods basically contain EKF [**?**], UKF [20], CDKF [21, 22], and CKF [23], where EKF is the most popular solution, and the later three are the so called sigma-point Kalman filter with higher computations and advanced performance. Same with complementary filters, Kalman filter is also often considered for attitude estimation. Sabatini presented his work to obtain accurate orientation estimation using EKF in [43]. To reveal higher accuracy, Marina proposed the attitude estimation algorithm based on UKF [35]. Although performance is guaranteed, these methods are heavy on computations, and resource constrained devices could not afford for it. Similar with the development trend of complementary filters, the problem of attitude estimation using Kalman filter are revisited recently. Valenti presented a linear Kalman filter (LKF) [44] using the algebraic quaternion algorithm. As well, Guo proposed the fast Kalman filter (Guo's FKF) [52] with their previous contributions, which has been proved to be better than LKF. These attempts exactly made a major breakthrough on reducing computational cost. However, existing solutions are

still not perfect. For example, too many linear approximations could lower the accuracy, and there may be alternative methods to further reduce the computational cost, and maintain the accuracy.

Therefore, what motivates us is to develop a novel lightweight Kalman estimator to reduce computational cost, and maintain the accuracy so as to further reduce power dissipation for MARG sensors attitude estimation. In this paper, a simplified measurement model is systematically derived to establish the LEKF with employing the quaternion kinematic equation as the process model. This proposed measurement model simplifies the involved computations, and is proved to make a contribution on reducing computation cost. During the experiments, a commercial sensor for data collection, and an optical system to provide reference measurements of orientation, namely Vicon, are utilized to investigate the performance of the established Kalman filter. Evaluation for different application scenarios is considered, which primarily include human motion capture and the drone applications. Results indicate that the proposed filter provides reliable performance for both applications. Moreover, the comparison experiment shows that the proposed filter provides better performance in terms of either attitude estimation accuracy or computational time.

This chapter is organized as follows. Section II involves the attitude determination from the accelerometer and magnetometer. Section III describes the design and implementation of the proposed filter. Experimental environment, experiments, and results are presented in Section IV. Section V gives the concluding remarks.

3.2 Orientation from Observation Vectors

This section deals with the orientation determination from the observers with the assumption that the observers are not influenced by any external disturbance. Given normalized observation vectors $A^b = (a_x, a_y, a_z)^T$, $M^b = (m_x, m_y, m_z)^T$ obtained from accelerometer and magnetometer respectively in the body frame, the orientation determination in the North-East-Down (NED) frame can be modeled by

$$\begin{aligned} A^b &= CA^r, \\ M^b &= CM^r, \end{aligned} \tag{3.1}$$

where C is theDCM, and $A^r = (0, 0, 1)^T$, $M^r = (m_N, 0, m_D)^T$ denote the reference vectors of earth gravitational and magnetic fields respectively, while m_D and m_N in [40] are computed by

$$\begin{aligned} m_D &= a_x m_x + a_y m_y + a_z m_z, \\ m_N &= \sqrt{1 - m_D^2}. \end{aligned} \tag{3.2}$$

As was discussed earlier, orientation determination from a set of vector observations is called Wahba's problem, there are amounts of solutions to this problem. Although methods such as QUEST, FOMA, and ESOQ guarantee the performance, these methods greatly increase the computational cost, and are commonly implemented for more than two observation vectors' systems. In our case, the sampling rate generally is synchronized with the gyroscope where only two vectors are involved, the earliest and simplest solution, TRIAD method, is sufficient, and taken into consideration, and we review the formula:

$$\begin{aligned} C &= M_o M_r^T, \\ M_o &= \left(o_1 | o_2 | o_3\right), \\ M_r &= \left(r_1 | r_2 | r_3\right), \end{aligned} \tag{3.3}$$

where the observation vectors o_i and the reference vectors r_i are computed by

$$\begin{aligned} o_1 &= W_1, \\ o_2 &= W_2, \\ o_3 &= W_1 \times W_2, \\ r_1 &= V_1, \\ r_2 &= V_2, \\ r_3 &= V_1 \times V_2. \end{aligned} \tag{3.4}$$

Directly, we assign (W_1, V_1) to the pair $\left(A^b, A^r\right)$, and (W_2, V_2) to the pair $\left(M^b, M^r\right)$. Through derivation, the final result C is given by

$$\begin{aligned} C &= \begin{pmatrix} C_{1,1} & C_{1,2} & C_{1,3} \\ C_{2,1} & C_{2,2} & C_{2,3} \\ C_{3,1} & C_{3,2} & C_{3,3} \end{pmatrix} \\ &= \begin{pmatrix} \frac{m_x - m_D a_x}{m_N} & \frac{a_y m_z - a_z m_y}{m_N} & a_x \\ \frac{m_y - m_D a_y}{m_N} & \frac{a_z m_x - a_x m_z}{m_N} & a_y \\ \frac{m_z - m_D a_z}{m_N} & a_x m_y - a_y m_x & a_z \end{pmatrix}, \end{aligned} \tag{3.5}$$

On another hand, considering the representation of elements of DCM in the form of

quaternion,

$$\begin{aligned}
C_{1,1} &= q_0^2 + q_1^2 - q_2^2 - q_3^2 \\
C_{1,2} &= 2(q_1 q_2 + q_0 q_3) \\
C_{1,3} &= 2(q_1 q_3 - q_0 q_2) \\
C_{2,1} &= 2(q_1 q_2 - q_0 q_3) \\
C_{2,2} &= q_0^2 - q_1^2 + q_2^2 - q_3^2 \\
C_{2,3} &= 2(q_0 q_1 + q_2 q_3) \\
C_{3,1} &= 2(q_0 q_2 + q_1 q_3) \\
C_{3,2} &= 2(q_2 q_3 - q_0 q_1) \\
C_{3,3} &= q_0^2 - q_1^2 - q_2^2 + q_3^2
\end{aligned} \tag{3.6}$$

and the transformation relation between the quaternion and the Euler angles,

$$\begin{aligned}
\phi &= atan2(2(q_0 q_1 + q_2 q_3), q_0^2 - q_1^2 - q_2^2 + q_3^2) \\
&= atan2(C_{2,3}, C_{3,3}) \\
\theta &= asin(2(q_0 q_2 - q_3 q_1)) \\
&= asin(-C_{1,3}) \\
\psi &= atan2(2(q_0 q_3 + q_1 q_2), q_0^2 + q_1^2 - q_2^2 - q_3^2) \\
&= atan2(C_{1,2}, C_{1,1})
\end{aligned} \tag{3.7}$$

where ϕ is the roll, θ for pitch, and ψ for yaw, respectively. Taking the constraint of the quaternion representing the orientation into consideration, we can obtain that using only four elements of the DCM are sufficient to extract the Euler angles, thereinto $C_{1,3}$ and $C_{2,3}$ are for determining the pitch and roll angles, and $C_{1,1}$ and $C_{1,2}$ are responsible for the yaw angle. Although $C_{3,3}$ as well can play the same role as $C_{1,1}$, $C_{1,1}$ is preferred because of the simpler calculations, as the following reformulated measurement model indicates.

$$\mathbf{z}_k = \begin{pmatrix} C_{1,3} \\ C_{2,3} \\ C_{3,3} \\ C_{1,2} \end{pmatrix} = \begin{pmatrix} a_x \\ a_y \\ a_z \\ \frac{a_y m_z - a_z m_y}{m_N} \end{pmatrix}, \tag{3.8}$$

Conspicuously, the derived measurement model involves a few computations, on the one hand, it is a low dimensional system, and easy to obtain the results given the measurements from the accelerometer and magnetometer, on the other hand, it is later proved that other involved computations are greatly reduced, particularly the computation of the Jacobian matrix of this model. What's more, the proposed measurement model is nonlinear, the good performance should be guaranteed in theory.

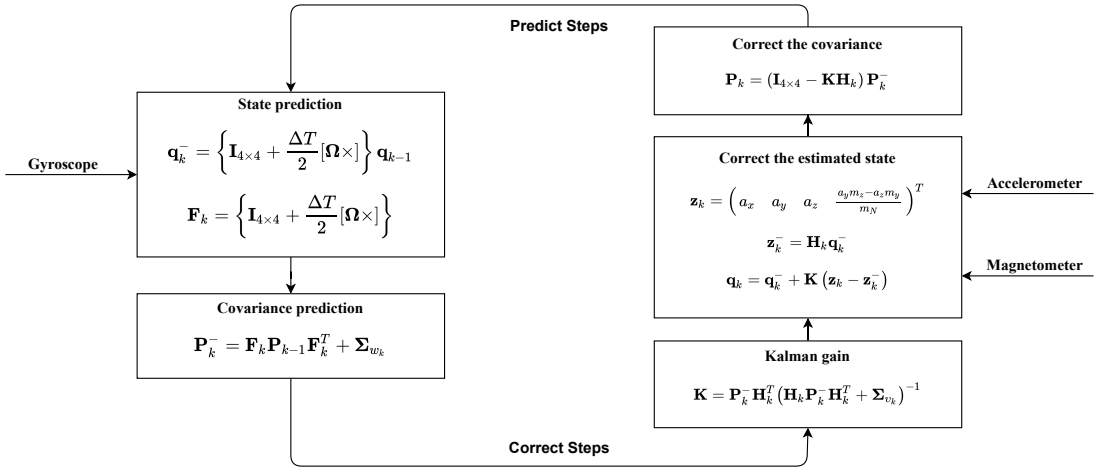

Figure 3.1: Workflow Diagram of the Proposed LEKF

3.3 Filter Design

This section investigates the establishment of the proposed LEKF, and we firstly assume that the bias error of gyroscope are constant, and has been cancelled before used. In order to formulate the system model, we employ the discretized quaternion kinematic equation as the process mode, which is written as

$$\mathbf{q}_k = \left\{\mathbf{I}_{4\times4} + \frac{\Delta T}{2}[\mathbf{\Omega}\times]\right\}\mathbf{q}_{k-1}, \tag{3.9}$$

where $\mathbf{q}_k = \begin{pmatrix} q_{0,k} & q_{1,k} & q_{2,k} & q_{3,k} \end{pmatrix}^T$ defines the process state in quaternion form at time k, $\mathbf{I}_{4\times4}$ is the 4×4 identity matrix, and ΔT denotes the sampling interval between epoch k and $k-1$, while $[\mathbf{\Omega}\times]$ is determined with the gyroscope output $\omega = (\omega_x, \omega_y, \omega_z)^T$ by

$$[\mathbf{\Omega}\times] = \begin{pmatrix} 0 & -\omega_x & -\omega_y & -\omega_z \\ \omega_x & 0 & \omega_z & -\omega_y \\ \omega_y & -\omega_z & 0 & \omega_x \\ \omega_z & \omega_y & -\omega_x & 0 \end{pmatrix}. \tag{3.10}$$

By integrating with the derived measurement model, the Kalman filter model is formulated by

$$\begin{aligned} \mathbf{q}_k &= \left\{\mathbf{I}_{4\times4} + \frac{\Delta T}{2}[\mathbf{\Omega}\times]\right\}\mathbf{q}_{k-1} + w_k, \\ \mathbf{z}_k &= \mathbf{H}_k\mathbf{q}_k + \upsilon_k, \end{aligned} \tag{3.11}$$

where w_k and υ_k denote the progress noise and observation noise respectively, while $\mathbf{H}_k$ is the observation matrice, we write down the derivation by

$$\begin{aligned}\mathbf{H}_k &= \frac{\partial \begin{pmatrix} 2q_{1,k}q_{3,k} + 2q_{2,k}q_{0,k} \\ 2q_{2,k}q_{3,k} - 2q_{1,k}q_{0,k} \\ q_{0,k}^2 - q_{1,k}^2 - q_{2,k}^2 + q_{3,k}^2 \\ 2q_{1,k}q_{2,k} - 2q_{3,k}q_{0,k} \end{pmatrix}}{\partial \mathbf{q}_k} \\ &= 2 \begin{pmatrix} -q_{2,k} & q_{3,k} & -q_{0,k} & q_{1,k} \\ q_{1,k} & q_{0,k} & q_{3,k} & q_{2,k} \\ q_{0,k} & -q_{1,k} & -q_{2,k} & q_{3,k} \\ q_{3,k} & q_{2,k} & q_{1,k} & q_{0,k} \end{pmatrix}.\end{aligned} \tag{3.12}$$

As is known, the process model and measurement model can not be applied to the covariance directly. Instead, the matrices of the Jacobian are computed, which are actually the partial derivatives for both models. For the process model, the Jacobian $\mathbf{\Xi}_{k-1}$ is given by

$$\mathbf{\Xi}_{k-1} = \begin{pmatrix} q_{1,k-1} & q_{2,k-1} & q_{3,k-1} \\ -q_{0,k-1} & q_{3,k-1} & -q_{2,k-1} \\ -q_{3,k-1} & -q_{0,k-1} & q_{1,k-1} \\ q_{2,k-1} & -q_{1,k-1} & -q_{0,k-1} \end{pmatrix}. \tag{3.13}$$

while the Jacobian $\mathbf{J}$ for the measurement model is derived by

$$\begin{aligned}\mathbf{J} &= \frac{\partial \mathbf{z}_k}{\partial \left\{ (\mathbf{A}^b)^T, (\mathbf{M}^b)^T \right\}} \\ &= \begin{pmatrix} \frac{\partial C_{1,3}}{\partial a_x} & \frac{\partial C_{1,3}}{\partial a_y} & \frac{\partial C_{1,3}}{\partial a_z} & \frac{\partial C_{1,3}}{\partial m_x} & \frac{\partial C_{1,3}}{\partial m_y} & \frac{\partial C_{1,3}}{\partial m_z} \\ \frac{\partial C_{2,3}}{\partial a_x} & \frac{\partial C_{2,3}}{\partial a_y} & \frac{\partial C_{2,3}}{\partial a_z} & \frac{\partial C_{2,3}}{\partial m_x} & \frac{\partial C_{2,3}}{\partial m_y} & \frac{\partial C_{2,3}}{\partial m_z} \\ \frac{\partial C_{3,3}}{\partial a_x} & \frac{\partial C_{3,3}}{\partial a_y} & \frac{\partial C_{3,3}}{\partial a_z} & \frac{\partial C_{3,3}}{\partial m_x} & \frac{\partial C_{3,3}}{\partial m_y} & \frac{\partial C_{3,3}}{\partial m_z} \\ \frac{\partial C_{1,2}}{\partial a_x} & \frac{\partial C_{1,2}}{\partial a_y} & \frac{\partial C_{1,2}}{\partial a_z} & \frac{\partial C_{1,2}}{\partial m_x} & \frac{\partial C_{1,2}}{\partial m_y} & \frac{\partial C_{1,2}}{\partial m_z} \end{pmatrix}\end{aligned} \tag{3.14}$$

The detailed results are listed in the Appendix **A**. Henceforth, we can easily handle the covariance $\mathbf{\Sigma}_{w_k}$ for the process noise, and $\mathbf{\Sigma}_{\upsilon_k}$ for the observation noise, which are respectively computed by

$$\mathbf{\Sigma}_{w_k} = \left(\frac{\Delta T}{2}\right)^2 \mathbf{\Xi}_{k-1} \mathbf{\Sigma}_{gyro} \mathbf{\Xi}_{k-1}^T, \tag{3.15}$$

and

$$\mathbf{\Sigma}_{\upsilon_k} = \mathbf{J} \cdot diag\left[\mathbf{\Sigma}_{acc}, \mathbf{\Sigma}_{mag}\right] \cdot \mathbf{J}^T, \tag{3.16}$$

where $\mathbf{\Sigma}_{gyro} = \sigma_g^2 \cdot \mathbf{I}_{3\times 3}$ is the covariance of gyroscope, $\mathbf{\Sigma}_{acc} = \sigma_a^2 \cdot \mathbf{I}_{3\times 3}$ for accelerom-

eter, and $\mathbf{\Sigma}_{mag} = \sigma_m^2 \cdot \mathbf{I}_{3\times3}$ for magnetometer, in general they can be obtained from the device specification directly.

At this point, we have completely described the derivation of the proposed LEKF. With the predict measurement $\mathbf{z}_k^-$ which is computed by

$$\mathbf{z}_k^- = \mathbf{H}_k \mathbf{q}_k^- \tag{3.17}$$

the workflow is summarized in Fig. 3.1. Considering the constraints of the quaternion representing the orientation and to ensure the filer working correctly, another thing that should be noted, is that the last resulting quaternion must be normalized in every iteration of Kalman filtering. Intuitively, LEKF is a lightweight Kalman filter, due to the simplified measurement model, and that its involved computation is reduced, particularly more than half elements of the Jacobian $\mathbf{J}$ are constant, and other parameters have plenty of common factors.

Figure 3.2: Experimental Devices: WitMotion HWT905 and NanoPi Duo2

3.4 Experiments and Results

In this section, we conduct several experiments to investigate the performance of the proposed LEKF. The detailed description about experimental setup and data collection is given in the first subsection.

3.4.1 Experimental environment and data collection

The experimental data for testing the filters is collected with a commercial sensor, namely WitMotion HWT905. HWT905 is a 10-axis orientation sensor with temperature compensation which contains 16 bit 3-axis gyroscopes, accelerometers and

magnetometers, and interfaced with a compact computer called NanoPi Duo2. The hardware is shown in Fig. 3.2. In the following experiments, the raw data is collected via the UART to USB data wire at 200Hz. With Zhang's contribution in [7], his proposed calibration method is employed to cancel the bias errors, including both of the accelerometer and the gyroscope, while the scale factor error, as the equation 5 indicates in [7], is not considerable in our case. Academically, the scale factor error also should be concerned for the calibration, yet it's experimentally proved to be extremely small [53,54], and have few influence comparing with the bias errors, especially for the sensor fusion of short time periods, and modern advanced integrated sensors. Regrading on the magnetometer, the frequently-used ellipsoid fitting algorithm is applied to calibrate the magnetometer [55]. Through analyzing the obtained calibration parameters, we found that the drone has a significant magnetic disturbance to the axis-z of the magnetometer, including both of the soft- and hard-iron interference, it is predictable that the angle of yaw could be subject to greater errors than other two of Euler angles. For the filter setup, the sensor noise characteristics are obtained directly from the official datasheet of HWT905, that is, $\mathbf{\Sigma}_{gyro} = 0.0025 \cdot \mathbf{I}_{3\times3}\,(^\circ/s)^2$, $\mathbf{\Sigma}_{acc} = 0.0001 \cdot \mathbf{I}_{3\times3}\,g^2$, and $\mathbf{\Sigma}_{mag} = 0.0004 \cdot \mathbf{I}_{3\times3}\,uT^2$.

Figure 3.3: Experimental Platform

In order to provide the reference measurements, an optical motion capture system called Vicon is utilized, which consists of 8 infrared cameras, and is able to track the position of optical markers continually. To successfully extract the orientation parameters, three optical markers are mounted on the top of the drone, while the experimental devices are fixed on the bottom the drone, as shown in Fig. 3.3. The position of the attached markers is measured with sampling rate of 200 Hz, and then we extract the reference orientation parameters by post-processing. However, due to that both systems for data collection have different coordinate systems and clock resources, we have to take two steps to align the coordinate systems and clocks of the two different systems. Firstly, we keep the drone stationary, obtain the corresponding orientation using

an advanced Kalman filter, cubature Kalman filter [23], and then figure out the offset between the two coordinate systems. Secondly, for each experimental data, we perform a cross-correlation of both angular rates of the two systems to figure out the time drift, as indicated in Fig. 3.4, where both angular rates have been aligned to the same coordinate system. In theory, the error of time synchronization is less than one sampling interval.

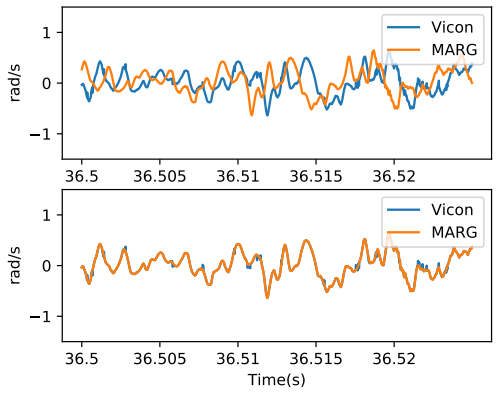

Figure 3.4: Unsynchronized and Synchronized Angular Rates

For the experiments, evaluation for different application scenarios is considered, which primarily includes human motion capture and the drone application. Both are the most common application scenarios almost covering all implementations in daily life, human motion capture applications usually behave very stochastically, thus haven't fixed characteristics in frequency domain, and demand more requirements on response accuracy, while the drone applications go along with relative regular high-frequency vibration and the magnetic disturbance, it might be the acid test of the robustness. For the assessment, no matter which application scenario, the performance evaluation will be reflected by the accuracy. In the case of human motion capture, the data is acquired from the motion randomly generated by moving the drone manually. For the drone application, the data is recorded during the real flight. All the experimental data are post-processed using python 3.7 on an Ubuntu 18.04 server with a CPU of 4-core i7-7700K. $\mathbf{q}_0 = \begin{bmatrix} 1 & 0 & 0 & 0 \end{bmatrix}^T$ and $\mathbf{P}_0 = 0.001 \cdot \mathbf{I}_{4\times4}$ are set as the initial conditions for the proposed filter.

3.4.2 Attitude estimation evaluation

Table. 3.1 shows the results of all the trials, where the upper three reflects the absolute accuracy for human motion capture, while the below three are the evaluation results of the drone during the real flight. For each trial, the attitude is calculated using LEKF proposed in the previous section, and the root-mean-square error (RMSE) is computed to measure the deference between the estimated Euler angles and the reference provided

Table 3.1: RMSE [in deg] of Attitude Estimation

Trials	Roll	Pitch	Yaw
1	1.28	1.60	3.01
2	1.16	0.95	2.87
3	0.82	0.90	2.82
4	1.27	1.05	6.37
5	1.13	0.94	4.04
6	1.48	2.01	8.41

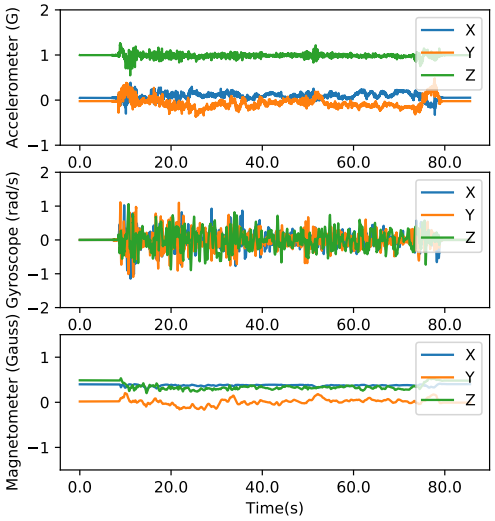

Figure 3.5: Raw Data of Trial1

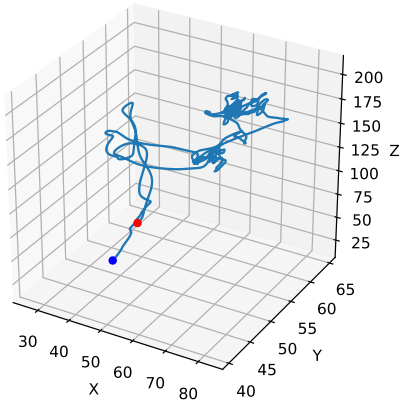

Figure 3.6: Consequent Movement of Trial1, Units: cm

by the optical system. Directly, although the movement range between different trials is different that leads to the fluctuating evaluation results, we can see that the estimated roll and pitch has relative stable performance for both application scenarios, whereas

the estimated yaw performs relatively poorly for human motion capture, and dramatically under the condition of drone applications. We would explain the results separately in detail in the following.

For more details about the attitude estimation for human motion capture applications, we show the raw data of the Trial1 in Fig. 3.5, the corresponding estimated Euler angles in Fig. 3.7, and the consequent moving trajectory in Fig. 3.6. Especially, Fig. 3.6 intuitively reveals the process of the movement, in which we pick up the sensor from the red point, then stochastically wave the sensor in the air, and finally put the sensor back to the blue position. In this case, the estimated Euler angles coincide well with the reference, except that the estimated yaw has a large initial error. Through our analysis, as stated above, the large initial error is caused by the significant magnetic distortion of the drone, even though the magnetometer's readings have been calibrated using ellipse fitting algorithm, it cannot be overcome completely. As well, the iron house, in which the optical system is assembled, has some effects on the magnetometer. This is why the estimated yaw performs a bit worse than the other two. In contrary, on the other hand, this proves that the proposed LEKF has a good convergence performance.

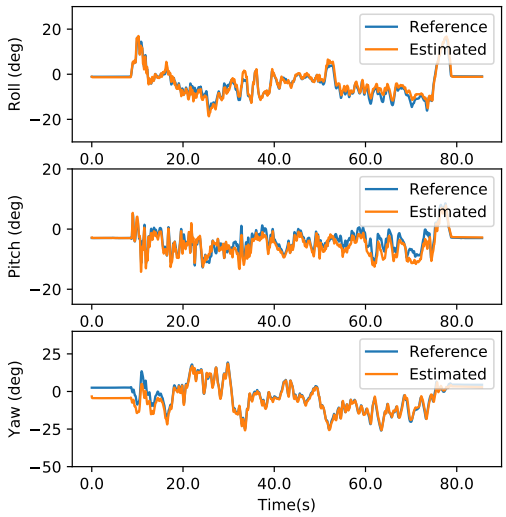

Figure 3.7: Estimated Euler Angles of Trial1

Similarly, in order to analyze the details about the attitude estimation for drone applications, Fig. 3.5 and Fig. 3.7 depict the raw data and corresponding estimated Euler angles of Trial4, respectively. For the large spikes of the raw data in the tail. it's attributed to the sudden landing of the drone. In this case, it can be recognized easily that there is drastic vibration on the axis-z of the accelerometer, which is certainly resulted by the flight of the drone. Even so, both of the roll and pitch still do the estimation very well. However, the estimated yaw diverges from the reference greatly. The reason is that the running motors of the drone, which always work with powerful

pulse current, further disturbs the surrounding magnetic field, it's very hard to deal with such dynamic noises. By contrast, the estimated roll and pitch angles are immune to the magnetic disturbance.

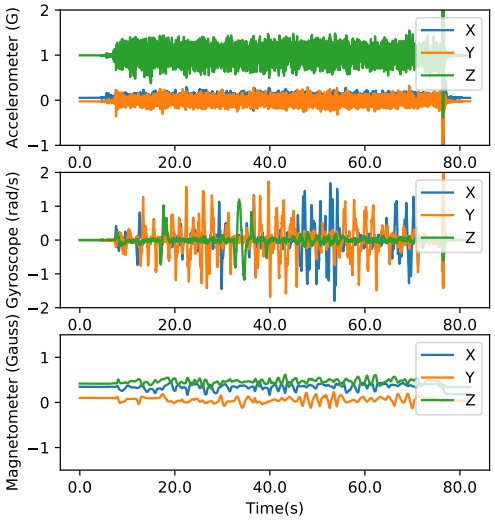

Figure 3.8: Raw data of Trial4

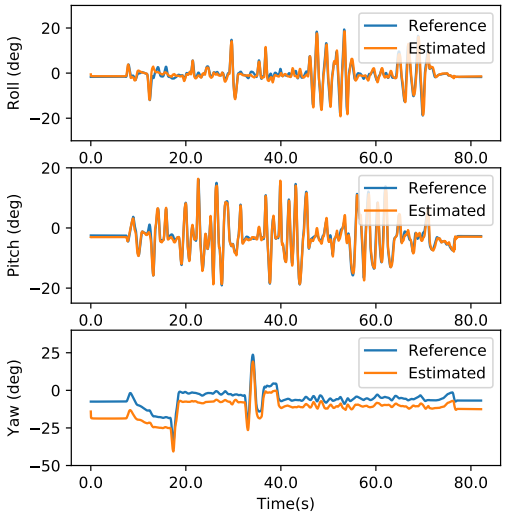

Figure 3.9: Estimated Euler Angles of Trial4

Evidently, through the evaluation results, the proposed LEKF is shown to coincide with the reference very well for both application scenarios. Although the performance of the estimated yaw depends on the environmental factor of the magnetic field strongly, the estimated roll and pitch are proved to be immune to the magnetic disturbance.

3.4.3 Robustness analysis

To verify the robustness of the proposed LEKF, the simulation experiments have been carried out. Normally, attitude estimation using MARG sensors has three factors of influence to the performance, that is, large external acceleration, magnetic disturbance, and high-frequency vibration of the drone applications. Generally, large external acceleration violates the assumption that the gravity is not distorted, and usually is solved with the basic idea that decrease the confidence interval of the accelerometer. However, in this article, the proposed LEKF does not involve the robust mechanism of large external accelerations, readers are referred to [**?**] for more details.

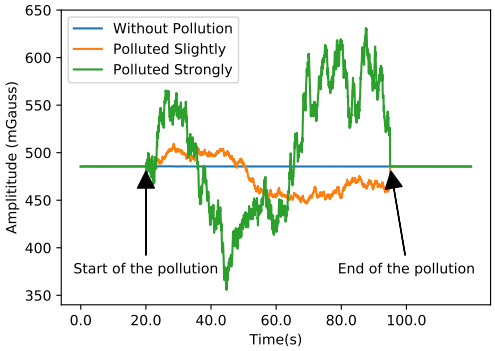

Figure 3.10: Norm of the Magnetic Field

When operating under the condition of the distorted magnetic field, the magnetometer's readings will be distorted heavily. To a certain degree, although the experiment of attitude estimation evaluation has proved the fact that the estimated roll and pitch are immune to the magnetic disturbance, to clearly learn the fact, a simulation is conducted where we distort the magnetometer's outputs manually. We collect a static data that is considered as a clean set of data, all the estimated Euler angles of which should stay in a straight line, and then manually pollute this data with both of soft- and hard-iron disturbance, as drawn in Fig. 3.10. Fig. 3.11 shows the estimated Euler angles of clean and polluted data for a comparison. Apparently, for the slight magnetic distortion (lower than 50 mGauss), basically we can say that the estimated roll and pitch are immune to the magnetic distortion. However, for the strong magnetic distortion (more than 50 mGauss), it not only affects the yaw angle but also the roll and pitch. In this case, a robust mechanism such as detecting the magnetic distortion with the norms of the magnetometer's readings can be leveraged to make all the Euler angles immune to magnetic disturbance.

Apart from the usual applications, attitude estimation on the drone has a high demand on the response in the presence of the vibration. As mentioned above, definitely there exists vibrations in all the trials of the drone, the Fast Fourier Transformation (FFT) analysis result, as shown in Fig. 3.12, also confirms it as fact, where an approxi-

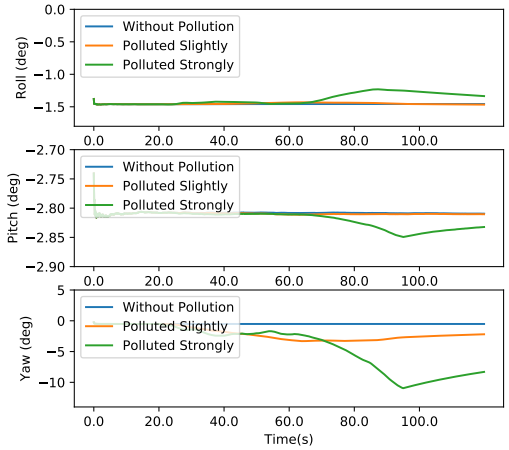

Figure 3.11: Estimated Euler Angles of Clean and Polluted Data

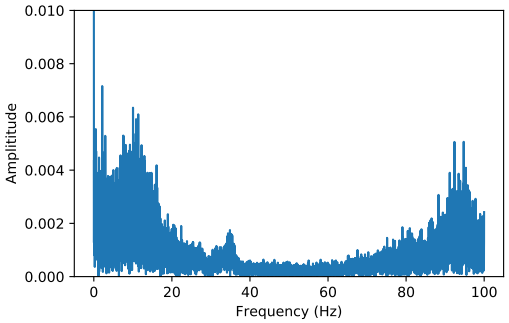

Figure 3.12: FFT Analysis Result of the Accelerometer‘s Axis-Z Values of Trial4

mate 90Hz vibration on the axis-z of the accelerometer's outputs can be identified easily. We can see that, although the proposed LEKF does not have any robust mechanism about the vibration, it's experimentally proved to have a good anti-vibration ability.

3.4.4 Comparison with representative kalman filters

In this subsection, we also assess the results from the representative Kalman filter, that is, the recent Guo's FKF [52], and the basic UKF which defines the system model as

$$\begin{aligned} \mathbf{q}_k &= \left\{ \mathbf{I}_{4\times 4} + \frac{\Delta T}{2}[\mathbf{\Omega}\times] \right\} \mathbf{q}_{k-1} + w_k, \\ \mathbf{z}_k &= \begin{bmatrix} A^b & M^b \end{bmatrix}^T \\ &= \mathbf{R}(\mathbf{q}_k^{-1}) \begin{bmatrix} A^r & M^r \end{bmatrix}^T + \upsilon_k^*. \end{aligned} \tag{3.18}$$

where the superscript of υ_k^* is utilized to distinguish with the proposed. Experimental conditions of which are the exact same as the LEKF, for instance the covariance of the filter, and the runtime environment. The experiment compares aspects of the precision of attitude estimation, and the computational cost.

Table 3.2: RMSE [in deg] of representative Kalman filters

Trials	RMSE			Method
	Roll	Pitch	Yaw	
1	1.60	1.68	3.22	Guo's FKF
	1.31	1.62	3.32	UKF
2	1.48	1.01	3.23	Guo's FKF
	1.17	0.98	2.49	UKF
3	1.20	0.95	3.22	Guo's FKF
	0.81	0.91	2.50	UKF
4	1.72	1.15	5.44	Guo's FKF
	1.23	1.03	5.87	UKF
5	1.25	0.92	2.44	Guo's FKF
	1.15	0.97	4.09	UKF
6	1.97	2.04	7.96	Guo's FKF
	1.41	1.95	5.87	UKF

The overall statistical values of the attitude estimation accuracy for all trials are shown in Table. 3.2, and Fig. 3.13 draws the estimation details of Trial1. Combining with Table. 3.1, we can find out that the accuracy of the proposed LEKF and the basic UKF has a tiny difference on the roll and pitch, on one hand, this is because the linearized system model limits the performance, so that the UKF cannot play to its strength, particularly for large nonlinear systems, on the other hand, this means that the proposed LEKF can provide excellent performance for such applications, as same as the UKF, although the EKF has first-order approximated the calculation progress. Also, we can see that, the proposed LEKF outperforms Guo's FKF on the estimation of roll and pitch, regardless of which application scenarios. Regarding the yaw angle, there are lots of uncertainties caused by the magnetic distortion, but in general, the proposed LEKF is second only to the UKF for human motion capture, it as well demonstrates that the UKF does well in challenging environment.

Computational cost is another important indicator of algorithm besides the accuracy. Here, we compare the consumed time of the proposed LEKF and Guo's FKF, whereas the UKF is not considered, due to UKF is an advanced Kalman filter, and normally takes much more computing time than EKF. The evaluation result is plotted in Fig. 3.14. Distinctly, the proposed LEKF is slightly faster than Guo's FKF.

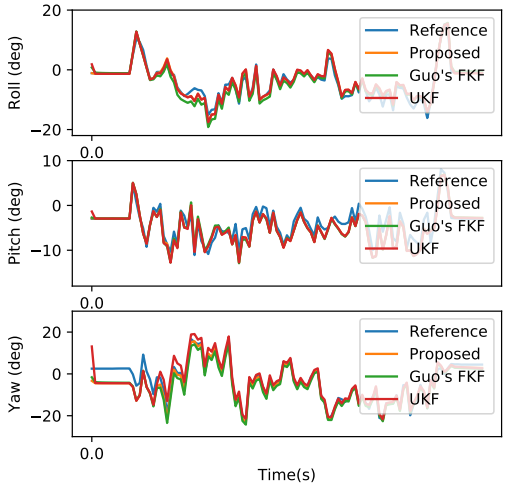

Figure 3.13: Estimated Euler Angles of Compared Filters

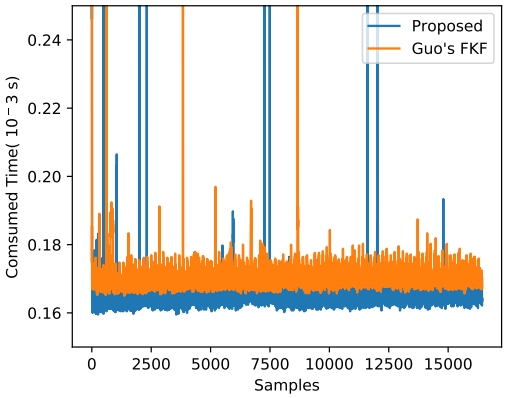

Figure 3.14: Consumed Time of the Proposed LEKF and Guo's FKF

3.5 Summary

Attitude estimation for MARG sensors is revisited in this work. With employing the quaternion kinematic equation as the process mode, we derive a simplified measurement model to establish the proposed LEKF. Our analysis prove that the proposed measurement model is conductive to reduce computation effort, this measurement model works efficiently, and simplifies the involved computation, especially the computation of its Jacobian where more than half elements are constant, and others have plenty of common factors.

Performance of the proposed LEKF are assessed using a commercial sensor for collecting raw MARG sensors' data and an optical system called Vicon to provide reference measurements. Evaluation for different application scenarios is considered, which primarily includes human motion capture and the drone application. Results indicate that the proposed LEKF performs very well, and is experimentally proved to have a

good anti-vibration. What's more, the estimated roll and pitch are immune to the relatively small magnetic distortion. Finally, the comparison experiment shows that the proposed LEKF can provide good performance, as same as the basic UKF, but it consumes slightly less time than Guo's FKF.

3.6 Appendix:Derivation of Jacobian Matrix

$$
\begin{aligned}
&\mathbf{J}_{1,1} = 1, \quad \mathbf{J}_{1,2} = 0, \quad \mathbf{J}_{1,3} = 0, \quad \mathbf{J}_{1,4} = 0,\\
&\mathbf{J}_{1,5} = 0, \quad \mathbf{J}_{1,6} = 0, \quad \mathbf{J}_{2,1} = 0, \quad \mathbf{J}_{2,2} = 1,\\
&\mathbf{J}_{2,3} = 0, \quad \mathbf{J}_{2,4} = 0, \quad \mathbf{J}_{2,5} = 0, \quad \mathbf{J}_{2,6} = 0,\\
&\mathbf{J}_{3,1} = 0, \quad \mathbf{J}_{3,2} = 0, \quad \mathbf{J}_{3,3} = 1, \quad \mathbf{J}_{3,4} = 0,\\
&\mathbf{J}_{3,5} = 0, \quad \mathbf{J}_{3,6} = 0,\\
&\mathbf{J}_{4,1} = \frac{-\frac{\partial m_N}{\partial a_x}(a_y m_z - a_z m_y)}{m_N^2},\\
&\mathbf{J}_{4,2} = \frac{m_z m_N - \frac{\partial m_N}{\partial a_y}(a_y m_z - a_z m_y)}{m_N^2},\\
&\mathbf{J}_{4,3} = \frac{-m_y m_N - \frac{\partial m_N}{\partial a_z}(a_y m_z - a_z m_y)}{m_N^2},\\
&\mathbf{J}_{4,4} = \frac{-\frac{\partial m_N}{\partial m_x}(a_y m_z - a_z m_y)}{m_N^2},\\
&\mathbf{J}_{4,5} = \frac{-a_z m_N - \frac{\partial m_N}{\partial m_y}(a_y m_z - a_z m_y)}{m_N^2},\\
&\mathbf{J}_{4,6} = \frac{a_y m_N - \frac{\partial m_N}{\partial m_z}(a_y m_z - a_z m_y)}{m_N^2}.
\end{aligned}
$$

where

$$
\begin{aligned}
&\frac{\partial m_D}{\partial a_x} = \frac{1}{2m_D} m_x, \quad \frac{\partial m_D}{\partial a_y} = \frac{1}{2m_D} m_y,\\
&\frac{\partial m_D}{\partial a_z} = \frac{1}{2m_D} m_z, \quad \frac{\partial m_D}{\partial m_x} = \frac{1}{2m_D} a_x,\\
&\frac{\partial m_D}{\partial m_y} = \frac{1}{2m_D} a_y, \quad \frac{\partial m_D}{\partial m_z} = \frac{1}{2m_D} a_z,\\
&\frac{\partial m_N}{\partial a_x} = -\frac{m_D}{m_N}\frac{\partial m_D}{\partial a_x}, \quad \frac{\partial m_N}{\partial a_y} = -\frac{m_D}{m_N}\frac{\partial m_D}{\partial a_y},\\
&\frac{\partial m_N}{\partial a_z} = -\frac{m_D}{m_N}\frac{\partial m_D}{\partial a_z}, \quad \frac{\partial m_N}{\partial m_x} = -\frac{m_D}{m_N}\frac{\partial m_D}{\partial m_x},
\end{aligned}
$$

$$\frac{\partial m_N}{\partial m_y} = -\frac{m_D}{m_N}\frac{\partial m_D}{\partial m_y}, \qquad \frac{\partial m_N}{\partial m_z} = -\frac{m_D}{m_N}\frac{\partial m_D}{\partial m_z}.$$

Chapter 4

Real-Time Attitude Estimation of Sigma-Point Kalman Filter via Matrix Operation Accelerator

4.1 Introduction

Low-cost MARG sensor array have been increasingly used to obtain precise attitude information. For example, accurate knowledge of attitude is essential for flight control in UAVs and mobile robotics navigation. Gyroscope measures the angular velocity of a moving object. Accelerometer and magnetometer measure the earth's gravitational and magnetic fields respectively to provide an absolute reference of orientation. As we known, these inexpensive sensors suffer from less accuracy and noisy due to white Gaussian noise and environmental effects like temperature or mechanical vibration. A lot of adaptive fusion techniques [39, 40, 42] have been studied in the past. In general we employ the well-known EKF [43, 52, 56] as the common solution.

However, the increasing demands for accuracy and robustness make us face greater challenges. The express companies are trying to use drones instead of people to delivery. More and more robots are being used for many tasks which are considered too dangerous for people to do. The harsh environment will lead to the highly nonlinear system. The EKF may not provide enough accuracy because of the limited first order accuracy of the nonlinear functions. The SPKF [57–59] is potentially better solution. The core of SPKF is the sigma-point approach, which propagates the sigma points through the true non-linearity, without approximation, and then a weighted mean and covariance is taken. This results in approximations that are accurate to the third order (Taylor series expansion) for nonlinear Gaussian inputs and at least the second-order for non-Gaussian inputs [60]. In addition, SPKF is free of the burdensome analytic derivation or Jacobians. Totally there are three kinds of SPKF, UKF [20], CDKF [21, 22]

and CKF [23]. Generally we use square-root filters because ill-conditioned covariance matrix may cause numerical instability. The only drawback is their higher computation cost than EKF. Typical embedded microprocessor can not afford for the real-time implementation.

To speed up such filters, many approaches using FPGA [61–64] have been proposed since matrix operations of these algorithms have high spatial and temporal parallelism. These method can be roughly divided into two categories. One is to implement the accelerator as the external co-processor. The other is to embed the accelerator in a soft-core processor and use custom instructions for accessing. More or less, methods are effective for acceleration compared with software implementation. However, it is easy to become obsessed with the acceleration and forget the re-usability. This will result in the waste of time for redesign, particularly when the design is quite complex.

Therefore, what motivates us is the re-usability. In this paper, an IP core called matrix operation accelerator is proposed, which not only can be reused to accelerate such matrix operation based filters, but also saves silicon. What's more, we implement the system on Zynq-7020 (XC7Z020-1CLG484) for experimental verification.

The organization of this chapter is as follows. First, we briefly introduce the algorithm of SPKF and sigma-point approaches in section 4.2. Then Section 4.3 describes the system architecture, including the filter design and the proposed matrix operation accelerator. The implementation of the system and evaluation about the result are presented in Section 4.4.2. Finally the work is concluded in Section 4.5.

4.2 Sigma-Point Kalman Filter

In this section, we briefly introduce SPKF, including the structure and methods to produce sigma points.

4.2.1 Filter structure

As with EKF, SPKF involves the estimation of the state of a discrete-time nonlinear dynamic system,

$$\begin{aligned} \mathbf{x_k} &= \mathbf{F}(\mathbf{x_{k-1}}, \mathbf{u_k}) + \mathbf{v_k} \\ \mathbf{y_k} &= \mathbf{H}(\mathbf{x_k}) + \mathbf{w_k} \end{aligned} \tag{4.1}$$

where $\mathbf{x_k}$ denotes the hidden state of the system, $\mathbf{u_k}$ is the control input and $\mathbf{y_k}$ represents the observed measurement at time $\mathbf{k}$. The state transition function $\mathbf{F}$ and observation function $\mathbf{H}$ are both nonlinear. The process noise $\mathbf{v_k}$ and the observation noise $\mathbf{w_k}$ are assumed to obey white Gaussian distribution, $N(0, Q_k)$ and $N(0, R_k)$ respectively. Furthermore, except the sigma-point approach, the framework of EKF and SPKF are

the exact same. Consequently we can summarize the structure of SPKF (UKF, CDKF and CKF) as,

Algorithm 1 Square-root sigma-point Kalman filter Structure

Initialize with

$$\hat{\mathbf{x}}_\mathbf{0} = \mathbf{E}\left[\mathbf{x_0}\right] \quad \mathbf{S_0} = chol\left\{\mathbf{E}\left[(\mathbf{x_0} - \hat{\mathbf{x}}_\mathbf{0})(\mathbf{x_0} - \hat{\mathbf{x}}_\mathbf{0})^T\right]\right\} \tag{4.2}$$

For $\mathbf{k} \in \{1, ..., \infty\}$,
Sigma-point calculation

$$\chi_{\mathbf{k-1}} = \text{sigma-function}(\hat{\mathbf{x}}_{\mathbf{k-1}}) \tag{4.3}$$

Time update

$$\begin{aligned}
\chi_{\mathbf{k|k-1}} &= \mathbf{F}(\chi_{\mathbf{k-1}}, \mathbf{u_{k-1}}) \\
\hat{\mathbf{x}}_\mathbf{k}^- &= \begin{cases} \sum_{i=0}^{2L} \omega_i^{(m)} \chi_{\mathbf{i,k|k-1}}, & \text{I} \\ \sum_{i=1}^{2L} \omega_i^{(m)} \chi_{\mathbf{i,k|k-1}}, & \text{II} \end{cases} \\
\mathbf{S}_\mathbf{k}^- &= qr\left\{\sqrt{\omega_i^{(c)}}(\chi_{\mathbf{1:2L,k|k-1}} - \hat{\mathbf{x}}_\mathbf{k}^-), \mathbf{S}_{Q,k-1}\right\} \\
\mathbf{S}_\mathbf{k}^- &= \begin{cases} cholupdate\left\{\mathbf{S}_\mathbf{k}^-, \chi_{\mathbf{0,k}} - \hat{\mathbf{x}}_\mathbf{k}^-, \omega_0^{(c)}\right\}, & \text{I} \\ \mathbf{S}_\mathbf{k}^-, & \text{II} \end{cases} \\
\mathcal{Y}_{k|k-1} &= \mathbf{H}(\chi_{\mathbf{k|k-1}}) \\
\hat{\mathbf{y}}_\mathbf{k}^- &= \begin{cases} \sum_{i=0}^{2L} \omega_i^{(m)} \mathcal{Y}_{i,k|k-1}, & \text{I} \\ \sum_{i=1}^{2L} \omega_i^{(m)} \mathcal{Y}_{i,k|k-1}, & \text{II} \end{cases}
\end{aligned} \tag{4.4}$$

Measurement update

$$\begin{aligned}
\mathbf{S}_{\hat{\mathbf{y}}_\mathbf{k}} &= qr\left\{\sqrt{\omega_i^{(c)}}(\mathcal{Y}_{1:2L,k|k-1} - \hat{\mathbf{y}}_\mathbf{k}^-), \mathbf{S}_{R,k-1}\right\} \\
\mathbf{S}_{\hat{\mathbf{y}}_\mathbf{k}} &= \begin{cases} cholupdate\left\{\mathbf{S}_{\hat{\mathbf{y}}_\mathbf{k}}, \mathcal{Y}_{0,k|k-1} - \hat{\mathbf{y}}_\mathbf{k}^-, \omega_0^{(c)}\right\}, & \text{I} \\ \mathbf{S}_{\hat{\mathbf{y}}_\mathbf{k}}, & \text{II} \end{cases} \\
\mathbf{P}_{\mathbf{x_k y_k}} &= \sum_{i=0}^{2L} \omega_i^{(c)} \left[\chi_{\mathbf{i,k|k-1}} - \hat{\mathbf{x}}_\mathbf{k}^-\right]\left[\mathcal{Y}_{i,k|k-1} - \hat{\mathbf{y}}_\mathbf{k}^-\right]^T \\
\mathbf{K} &= (\mathbf{P}_{\mathbf{x_k y_k}} / \mathbf{S}_{\hat{\mathbf{y}}_\mathbf{k}}^\mathbf{T}) / \mathbf{S}_{\hat{\mathbf{y}}_\mathbf{k}} \\
\hat{\mathbf{x}}_\mathbf{k} &= \hat{\mathbf{x}}_\mathbf{k}^- + \mathbf{K}(\mathbf{y_k} - \mathbf{y}_\mathbf{k}^-) \\
\xi &= \sqrt{\omega_i^{(c)}}\left\{(\chi_{\mathbf{1:2L,k|k-1}} - \hat{\mathbf{x}}_\mathbf{k}^-) - \mathbf{K}(\mathcal{Y}_{1:2L,k|k-1} - \hat{\mathbf{y}}_\mathbf{k}^-)\right\} \\
\mathbf{S_k} &= \begin{cases} cholupdate\left\{\mathbf{S}_\mathbf{k}^-, \mathbf{K}\mathbf{S}_{\hat{\mathbf{y}}_\mathbf{k}}, -1\right\}, & \text{I} \\ qr\left\{\xi, \mathbf{S}_{R,k-1}\right\}, & \text{II} \end{cases}
\end{aligned} \tag{4.5}$$

where I for UKF and CDKF, II for CKF

As mentioned above, we use square-root filters to improve the numerical stability because all the covariance matrices are guaranteed to stay positive semi-definite. The square-root and non square-root filters are algebraically equivalent.

4.2.2 Sigma-point approach

The sigma-point approach is the core of SPKF. They are all related through making use of a technique called weighted statistical linear regressions to calculate the optimal terms in the Kalman update step. The different sigma-point approaches define different functions to produce sigma points.

In UKF, a set of sigma points is produced by the unscented transformation, which is formulated as,

$$\chi_{\mathbf{i,k-1}} = \begin{cases} \hat{\mathbf{x}}_{\mathbf{k-1}}, & i = 0 \\ \hat{\mathbf{x}}_{\mathbf{k-1}} + \sqrt{L+\lambda}(\mathbf{S_k})_i, & i = 1, ..., L \\ \hat{\mathbf{x}}_{\mathbf{k-1}} - \sqrt{L+\lambda}(\mathbf{S_k})_i, & i = L+1, ..., 2L \end{cases} \tag{4.6}$$

where L is the dimension of $\mathbf{x}$ and $(\mathbf{S_k})_i$ indicates the ith column of the matrix $\mathbf{S_k}$. Then we calculate the utilized weights by

$$\begin{aligned} \omega_0^{(m)} &= \frac{\lambda}{L+\lambda} & \omega_0^{(c)} &= \frac{\lambda}{L+\lambda} + (1 - \alpha^2 + \beta) \\ \omega_i^{(m)} &= \omega_i^{(c)} = \frac{1}{2(L+\lambda)} & i &= 1, ..., 2L \end{aligned} \tag{4.7}$$

where $\lambda = \alpha^2(L+k) - L$ is a scaling parameter. k is the secondary scaling parameter. α determines the spread of sigma points around $\mathbf{x}_k$ and is usually set to a small positive value $(0 \leq \alpha \leq 1)$. β incorporate prior knowledge of the distribution of $\mathbf{x}_k$. For Gaussian distributions, $\beta = 2$ and $k = 0$ is optimal [65].

The CDKF expands the nonlinear function by using Stirling's polynomial interpolation formula. Similar to UKF, the $(2L+1)$ sigma points and weights are produced by

$$\chi_{\mathbf{i,k-1}} = \begin{cases} \hat{\mathbf{x}}_{\mathbf{k-1}}, & i = 0 \\ \hat{\mathbf{x}}_{\mathbf{k-1}} + h(\mathbf{S_k})_i, & i = 1, ..., L \\ \hat{\mathbf{x}}_{\mathbf{k-1}} - h(\mathbf{S_k})_i, & i = L+1, ..., 2L \end{cases} \tag{4.8}$$

and

$$\begin{aligned} \omega_0^{(m)} &= \frac{h^2 - L}{h} & \omega_i^{(m)} &= \frac{1}{2h} \\ \omega_i^{(c)} &= \frac{1}{4h^2} & \omega_i^{(m)} &= \frac{h^2 - 1}{4h^2} \quad i = 1, ..., 2L \end{aligned} \tag{4.9}$$

Comparing with UKF, it's obvious that the CDKF uses only a single parameter, which is easy to tune from a practical perspective. Another advantage over UKF is the CDKF is more adaptive, they have the same performance though [22] [66].

The CKF employs a third-degree spherical-radical cubature rule to compute Gaussian-weighted integrals numerically with the best performance of them. The sigma-point approach is described by

$$\chi_{\mathbf{i,k-1}} = \begin{cases} \hat{\mathbf{x}}_{\mathbf{k-1}} + \sqrt{L}(\mathbf{S_k})_i, & i = 1, ..., L \\ \hat{\mathbf{x}}_{\mathbf{k-1}} - \sqrt{L}(\mathbf{S_k})_i, & i = L+1, ..., 2L \end{cases} \tag{4.10}$$
$$\omega_i^{(m)} = \omega_i^{(c)} = \frac{1}{2L}, i = 1, ..., 2L$$

Since CKF only requires $2L$ cubature points, CKF has better computational speed theoretically. It's more convenient to be implemented without free parameters to tune.

4.3 System Architecture Overview

Overview of the system architecture is given in this section. At first, we deal with the filter design, and then, we describe the details of the proposed matrix operation accelerator.

4.3.1 Filter design

Figure 4.1: Framework of 9-axis AHRS

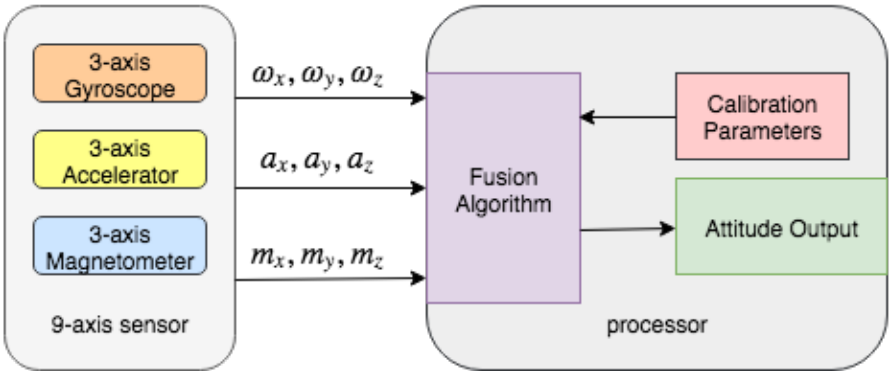

The general framework of 9-axis AHRS is shown in Fig. 4.1. We assume that biases of gyroscope, accelerometer and magnetometer are constant and cancelled before used. Moreover, quaternion is chosen as the attitude representation for solving gimbal lock and the computation simplicity. With the sensed angular rate $\omega = (\omega_x, \omega_y, \omega_z)^T$, we can

define the process model using the discretized quaternion kinematic equation,

$$\mathbf{q_k} = \left\{ \mathbf{I}_{4\times 4} + \frac{\Delta t}{2}[\mathbf{\Omega}\times] \right\} \mathbf{q_{k-1}} \tag{4.11}$$

where Δt denotes the sampling interval and

$$[\mathbf{\Omega}\times] = \begin{pmatrix} 0 & -\omega_x & -\omega_y & -\omega_z \\ \omega_x & 0 & \omega_z & -\omega_y \\ \omega_y & -\omega_z & 0 & \omega_x \\ \omega_z & \omega_y & -\omega_x & 0 \end{pmatrix} \tag{4.12}$$

With normalized observed vectors $A_b = (a_x, a_y, a_z)^T$, $M_b = (m_x, m_y, m_z)^T$ from accelerometer and magnetometer in body frame b, we formulate the measurement model by,

$$\mathbf{y_k} = \begin{bmatrix} A_b & M_b \end{bmatrix}^T = \mathbf{Rot}(\mathbf{q_k}) \begin{bmatrix} A_r & M_r \end{bmatrix}^T \tag{4.13}$$

where r indicates the reference frame and $\mathbf{Rot}(\mathbf{q_k})$ is the rotation matrix converted from $\mathbf{q_k}$, while A_r and M_r in [40] are given by

$$\begin{aligned} A_r &= \begin{bmatrix} 0 & 0 & 1 \end{bmatrix}^T \\ M_r &= \begin{bmatrix} m_N & 0 & m_D \end{bmatrix}^T \\ m_D &= a_x m_x + a_y m_y + a_z m_z \\ m_N &= \sqrt{1 - m_D^2} \end{aligned} \tag{4.14}$$

4.3.2 Matrix operation accelerator

Through analyzing the structure of SPKF, apparently it's a matrix operation based algorithm. These matrix operations include such like matrix inversion, matrix multiplication and qr decomposition and etc. Furthermore, the matrix operations are sequential, it's not necessary to synthese the whole algorithm to digital circuit, which is a very costly waste of silicon. As so, we design the matrix operation accelerator instead. It not only saves silicon but also is reusable to adapt for different matrix operation based algorithms. Fig. 4.2 shows the block of the matrix operation accelerator.

This block is able to manipulate the memory directly and works like Direct memory access (DMA). There are several registers in control unit, which is used to configure the matrix operation unit. Once we configure these registers by accessing the interface **ctrl**, this accelerator will automatically finish the matrix operation and move the resulting matrix to the destination memory area. Then, it will trig **irq_done** signal to inform other processing unit.

Figure 4.2: Block of the Matrix Operation Accelerator

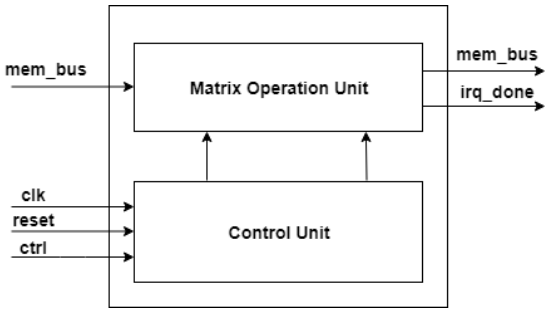

4.4 Implementation and Evaluation

In this section, we realize the matrix operation accelerator and evaluate the implementation on Zynq-7020 (XC7Z020-1CLG484). We first introduce the performance metrics. Then we discuss the experiment setup and evaluation results.

4.4.1 Performance metrics

We introduce one metric called speedup of the execution to evaluate the performance of the accelerator. The speedup of the execution is used to evaluate the improvement of the execution. Adapting the formula of Amdahl's law [67] to our system, the speedup of the execution can be obtained by

$$Speedup = t_{sw}/t_{hw} \tag{4.15}$$

where t_{sw} is the execution time of the software implementation and t_{hw} is the execution time of the accelerated implementation.

Figure 4.3: Architecture of the Experiment Platform

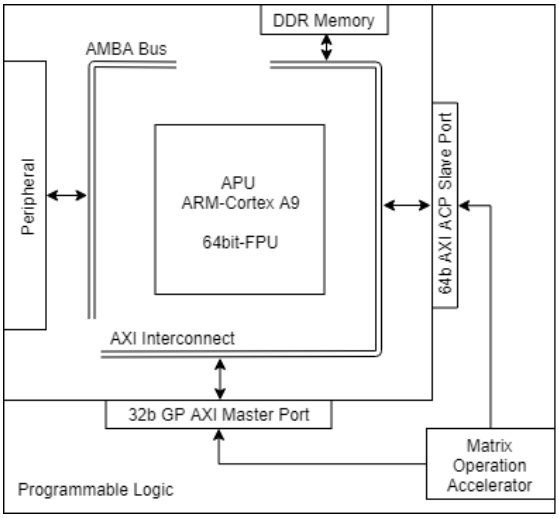

4.4.2 Experiment setup

The experiment is conducted on Zynq-7020 (XC7Z020-1CLG484), which is a mixed CPU-FPGA platform. Fig. 4.3 shows the whole architecture adapting for our evaluation. This device combines Programmable logic (PL) with Processing system (PS). PS is a dual-core ARM Cortex-A9 processing system and each of them is equipped with a single and double precision Vector floating point unit (VFPU).

In this experiment, the accelerator is programmed in C and synthesized using Xilinx's Vivado Design Suite for C-based implementation. To meet the requirement of precise, all operations implement double floating point arithmetic. There are two advanced extensible interface (AXI) between ARM and the accelerator. One is 32-bit general purpose AXI master port for configuring the accelerator, playing a role of **ctrl**. The other is 64-bit AXI accelerator coherency port (ACP) slave port enabling coherent accesses from PL to CPU memory space, as the **mem_bus**. Once configured, the accelerator will automatically manipulate the memory and finish data computation. For the evaluation, we configure the accelerator running at 100MHz and use single ARM Cortex-A9 core with enabled VFPU configured at 667MHz for performance comparison. And we set the dimension of all matrices to 14 according to the requirement of the implementation.

4.4.3 Performance of proposed accelerator

Totally six different matrix operations are synthesized into the PL. Table 4.1 shows the synthesis results, including the number of used resource and the utilization of PL. As seen from the table, only qr decomposition and $cholupdate$ use a little more resources than other operations, that is because this two operations involve more complex computation. The last term of this table shows the total used resource of the accelerator.

Table 4.1: Resource Utilization of Matrix Operation Accelerator

Operation Name	Number of resource utilization (%)			
	BRAM	DSP	FF	LUT
Add/Sub	2(0.7)	3(1.4)	805(7.6)	1348(2.5)
Dot	0(0)	28(12.7)	5253(4.9)	4584(8.6)
Invert	4(1.4)	39(17.7)	3091(2.9)	4326(8.1)
QR	4(1.4)	28(12.7)	11652(11.0)	15238(28.6)
Cholupdate	0(0)	25(11.4)	10956(10.3)	13743(25.8)
Total	24(8.6)	67(30.5)	28549(26.8)	33554(63.1)

Table 4.2 shows the latency of the accelerator and speedup of the execution. The speedup indicates the acceleration factor defined as the ratio of execution time of the software implementation to the execution time with the accelerator. From the table, the

matrix addition, subtraction and $cholupdate$ is slower than the software implementation when executing with the accelerator. The first two is because of the low computational complexity. $cholupdate$ is due to the sequential order of the calculations which can not be paralleled.

Table 4.2: Calculation Cycles and Speedup of Matrix Operation

Operation Name	Latency		Interval		Speedup
	Min	Max	Min	Max	t_{sw}/t_{hw}
Add/Sub	205	205	205	205	0.75
Dot	1406	1406	1406	1406	5.48
Invert	1124	9552	1124	9552	3.80
QR	3041	23971	3041	23971	1.65
Cholupdate	2482	2482	2482	2482	0.78

4.4.4 Performance of accelerated filters

In this part, we do the performance comparison of unaccelerated and accelerated SPKF. The test data is stored in the Secure digital card (SD card) and accessed by the Secure digital input output bus (SDIO bus). From the Table 4.3, it's obvious that the accelerator improves approximately 2 times the processing speed of SPKF.

Table 4.3: Execution Time of Square-Root SPKF in One Iteration

Filter	software implementation (msec)	with accelerator (msec)	speedup
UKF	2.22	1.32	168%
CDKF	2.34	1.25	187%
CKF	2.47	1.10	225%
Average	2.34	1.22	192%

4.5 Summary

In this chapter, a matrix operation accelerator is proposed to accelerate SPKF for real-time orientation estimation. These advanced filters have higher performance in terms of accuracy and more robust than EKF. It's quite essential for modern applications particularly in hash environment. The accelerator is programmed in C and synthesized using Xilinx's Vivado Design Suite. We conduct the experiment on Zynq-7020 (XC7Z020-1CLG484). The experimental results show that the accelerator is efficient of the computation and saves silicon. With this, on one hand, it not only improves the performance but also offloads the heavy computation from the CPU. On the other hand, it's reusable to speedup other matrix operation based algorithms, which will save

time for redesign. Although some of computation of SPKF is executed in software and can not be solved as the matrix operation, the proposed scheme is still a considerable solution to the problem of algorithm acceleration.

Chapter 5

Wireless Time Synchronized Motion Trackers Using Kalman Filtering to Multi-rate Sensor Fusion

5.1 Introduction

As discussed before, Motion capture (MoCap) technology has become increasingly popular and can be found everywhere in daily life. For example, in areas such as film and game industry, medical science and gesture recognition. In the film and game industry, the designers generally combine MoCap with virtual reality technology to make objects extremely vivid and lifelike [68]. Well-known film "Avatar" and game "Pokemon Go" have acquired a good reputation. In the filed of medical science, it's proved that MoCap is a good way of the monitoring of patients' condition and help them to obtain more efficient rehabilitation therapies [69, 70]. For gesture recognition, it's exactly an old research topic and improves users experience of human-computer interaction [71, 72]. Anyway, all the applications need obtain the positions, speeds, attitudes of the object by employing a certain MoCap technology.

As so far, there are many MoCap techniques that have been developed and only two of them become the promising frontier, namely, optical sensor based and MARG sensors based methods. Solutions such as mechanical based [73] and magnetic based [74–76] are being retired due to either the inconvenience for wearing or the low performance in terms of accuracy, while vision based method [77] is more susceptible to background, like illumination, occlusion and other environmental factors. Optical sensor based systems like Vicon [78] succeed in doing this and could be the first successful application of MoCap, which enable users to move freely and have an excellent performance on accuracy. Usually the users are required to wear infrared reflective markers and the system determines the motion of the markers from the images recorded by the

surrounding cameras. On the other hand, MARG based systems [79–81] extract the information by integrating the measurements of the gyroscope with a given initial condition or deriving from the two observed vectors referring to the global frame. However, optical based methods are only available in structured environments and quite expensive, it would be preferred for film shooting and other applications that require high accuracy. In comparison, MARG based systems are a very promising frontier because of its low price, low power consumption and small size, what's more, they can be used almost anywhere. In consequence, we focus on MARG based techniques for motion capture in this paper.

As we known, due to the bottleneck of each component of MARG, the MARG based systems have to employ the optimal sensor fusion algorithm to extract the accurate attitude information. These algorithms can generally be divided into two categories in rough; complementary filter CF based approaches and extended Kalman filter (EKF) based approaches respectively. Comparing with EKF based approaches, CF based approaches obtain the attitude by compensating for each other in the frequency domain. During the recent years, several advanced CF based methods have been developed. In [39], Madgwick proposed a computationally efficient orientation algorithm using the gradient descent algorithm. In 2016, Wu proposed a novel fast quaternion-based estimator to further reduce the computing complexity in [40]. Although CF has more efficient computations, a typical drawback is that the gain is constant and always empirically given for one time and the inability to adapt the weight for another quite different scenario. In contrast, EKF is always taken as the common solution due to the guaranteed high performance. In 2005, Trawny proposed an IKF [42] to solve the problem of attitude estimation. This approach performs well on robustness and still provides a reference of the idea for the modern applications. To reduce the computational complexity, Valenti presented a linear Kalman filter using the algebraic quaternion algorithm in [44], and Guo established a more computational measurement model in his proposed FKF respectively. These work proved that EKF is adaptive and has a stable performance on accuracy. Therefore, we employ EKF as the solution of attitude estimation as well.

Until now, many motion capture systems have already been developed [24, 79, 81, 82], especially the famous commercial motion capture system Xsens MVN [24] has been wildly used in the practical applications. Commercial systems, although being easy-to-use and providing an excellent performance in terms of accuracy, strictly limit the scalability of the sensor network because the sensor network is established using their self-defined protocol. Moreover, the time synchronization of the asynchronous network often has been ignored. Even the company Xsens handled the problem by the hardware solution in the next generation product [82] and achieved high accuracy of time synchronization, the hardware method is quite expensive and exceeds the actual need. For the prototypes developed by the research center, they normally focused on re-

ducing the limitations such as power consumption, size and weight, it is rate to consider the scalability and time synchronization of the sensor network of the motion capture system.

Therefore, the novel wireless time synchronized motion tracker is proposed in this chapter. The presentation will be described in three aspects: the working principles of the motion tracker, the design of the attitude estimation algorithm and the validation of the motion tracker.

5.2 Work Principles

In this section, the working principles of the proposed motion tracker are introduced in detail, including the architecture of the tracker, the establishment of the motion capture system and segment kinematics. As well as the facing problems, time synchronization of trackers in an asynchronous sensor network are investigated.

5.2.1 Motion tracker overview

Fig. 5.1 shows the prototype of the motion tracker, which is a small embedded system with a package size of 47mm(W)×30mm(D)×13mm(H) (excluding the mounting ear) and a weight of 26g. It is powered using a LiPo battery and lasts for more than 2h at least in the real test. Fig. 5.2 shows the diagram of the motion tracker. Each tracker is composed of a microcontroller that has a built-in Wireless Fidelity (Wi-Fi) connectivity and a low-cost inertial and magnetic measurement unit that consists of 3-axis accelerometer, 3-axis gyroscope and 3-axis magnetometer. Gyroscope senses the angular rate in three axis and provides an estimate of the orientation when integrated with previous orientation state over time. Accelerometer and magnetometer measure strength and direction of the reference field, gravity and magnetic field respectively. In the context of sensor fusion, a quaternion-based EKF to multi-rate sensor fusion is proposed as the reliable solution and eliminates the bottleneck of each single sensor. This fusion algorithm enables the sensors working at an asynchronous measurement rate and takes full advantage of the performance of all the sensors. In the course of the tracker work, the microcontroller acquires the measurement from the sensing elements, process the data using our proposed EKF, and transfer the results out through the wireless network. Besides, the Micro-USB interface driven by the terminal program is provided to configure the working parameters of the tracker, such as the sampling rate, the measurement rage and so on. The major configurable parameters are list in Table. 5.1.

For the program residing in the microcontroller, totally three tasks are created and running on a mini real-time kernel FreeRTOS. The first task is designed to acquire the

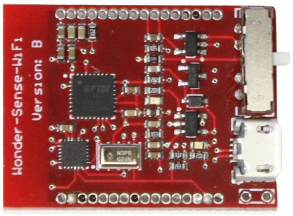

(a) Hardware Top View

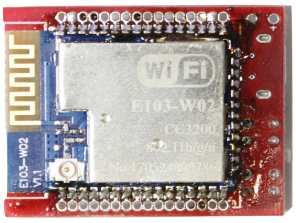

(b) Hardware Bottom View

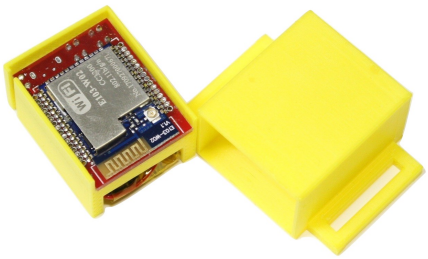

(c) Tracker Inside View

(d) Tracker Prototype

Figure 5.1: Overview of the Motion Tracker Prototype

Table 5.1: Major configurable parameters of the tracker

	Available Configurations	Units
Full-Scale Range		
Gyroscope	$\pm 250, \pm 500, \pm 1000, \pm 2000$	$^\circ/s$
Accelerometer	$\pm 2, \pm 4, \pm 8, \pm 16$	g
Magnetometer	± 4800	μT
Others		
Low Pass Filter	$5, 10, 20, 41, 92, 184$	Hz
Output Rate	$0 \sim 100$	Hz

measurement from the motion sensor and estimate the attitude using our proposed EKF. Further, the processed data is delivered to the second task, which actually is a client program using Transmission Control Protocol/Internet Protocol (TCP/IP) and transfers the results out. Last but not least, the third task runs a terminal program for human computer interaction to configure the parameters of the motion tracker. These tasks ensure that the motion sensing will be completed successfully.

On the whole, the proposed motion tracker is compact and easy in implementation.

5.2.2 Motion capture system

Except the motion trackers, we need a wireless router and a computer that is able to run a server program of TCP/IP to establish the motion capture system. Evidently, the scalability of the sensor network just depends on the performance of the router and the computer. In other word, the scalability is not limited by the data transmission protocol

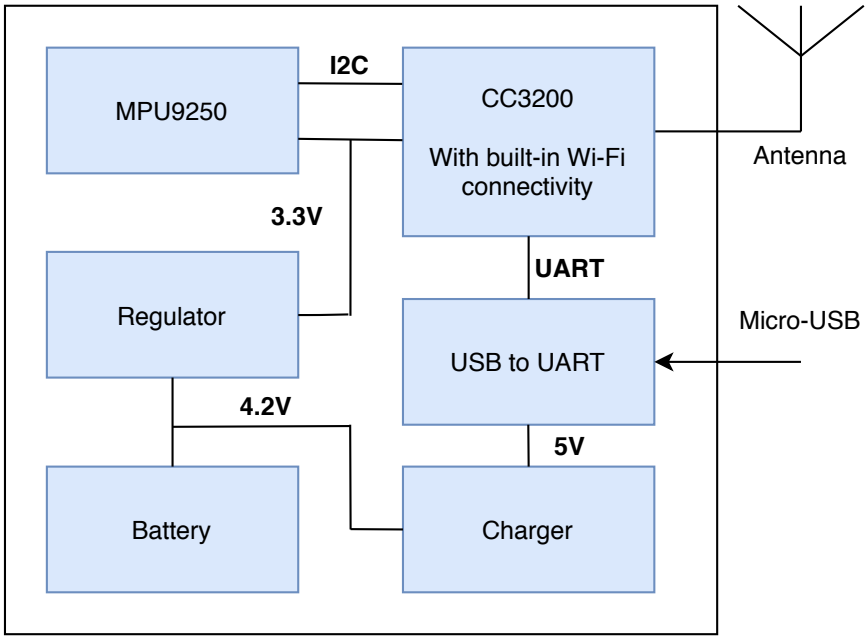

Figure 5.2: Block Diagram of the Motion Tracker

of the motion tracker and it doesn't take much effort to remove or add a tracker node. However, one coin has two sides. The built sensor network is asynchronous. This is to say, the measurements are misaligned from different trackers, and we have to figure out a solution for the time synchronization before conducting any motion tracking activities.

Note that the gyroscope will produce the same results when placed in the same coordinate system, this property can be utilized to figure out the problem of time synchronization. We assume that all the sensors hold the same characteristics particularly the sampling interval. In the beginning of conducting the motion capture, we attach all the required trackers to the same rigid segment and perform some random acts for a while. We choose one of them as the benchmark, find other trackers to the benchmark alignment and rotate all the angular rate to the coordinate system of the benchmark. Theoretically all the results should be the almost same. With the symbol ${}^j_i\mathbf{q}$ to express the rotation from the frame of the tracker i to the frame of the benchmark tracker j, such rotation operation can be formulated by

$$ {}^j\omega = {}^j_i\mathbf{q} \otimes {}^i\omega \otimes {}^j_i\mathbf{q}^*, \quad i \neq j \tag{5.1} $$

where $\otimes$ denotes the quaternion product and $*$ is the conjugate of the quaternion [3], while ${}^i\omega$ indicates the angular rate of the tracker i. In this way, choosing any one of them as the benchmark, we can perform a cross-correlation to figure out the time offset. In theory, the time synchronization error is lower than one sampling interval of the gyroscope. The higher sampling rate is conducive to improve the time synchronization accuracy.

Although the method for time synchronization adds the complexity of the usage in some way, it is acceptable and easy to operate. In particular, this approach reduces the cost and avoids the complicated hardware design.

5.2.3 Segment kinematics

Each subject body contains body segments which are linked by the joints. When the trackers are attached to the subject's body segments, segment kinematics actually is the translation from the tracker kinematics to body segment kinematics using a bio-mechanical model. In this way, the translation will be a two-step process. The first step is to align the sensor with the segment, in other word, the system calibration. Usually, similar to other researchers, the well-known T-pose and N-pose are considered as the solution. This asks the subject to stand like that for a while, the translation from the tracker to the body segment ${}^{B}_{S}\mathbf{q}$ will be determined by

$$ {}^{G}_{B}\mathbf{q} = {}^{G}_{S}\mathbf{q} \otimes {}^{B}_{S}\mathbf{q}^{*} \tag{5.2} $$

where ${}^{G}_{B}\mathbf{q}$ is the known orientation of each segment in T-pose or P-pose. In fact, different applications require different calibration methods, more detailed information is provided in [24, 83].

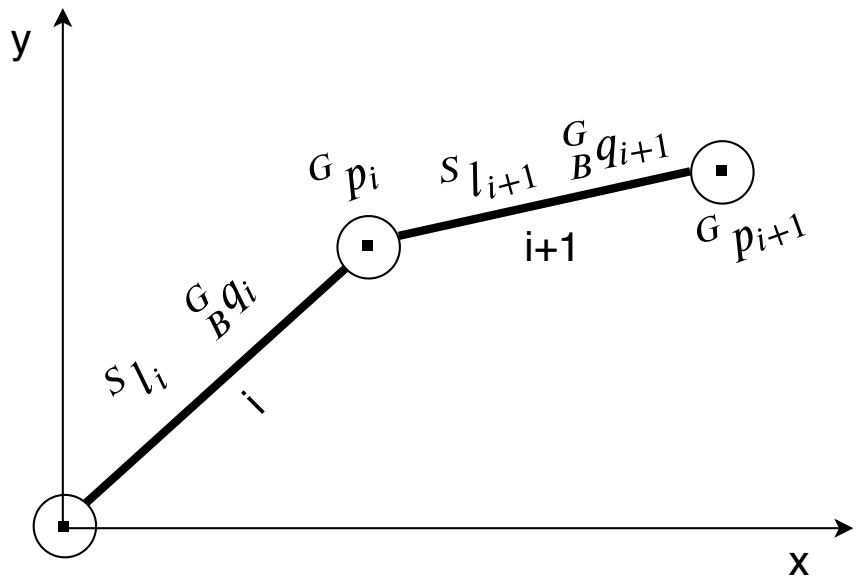

Figure 5.3: Schematic of Segment Kinematics

The second step is to figure out the way to update the position of the joint. Fig. 5.3 shows the simplified schematic of segment kinematics in the global two-dimensional coordinate system. Evidently, the position ${}^{G}p_{i+1}$ is determined by the translation of the position ${}^{G}p_{i}$ and the rotation ${}^{G}_{B}\mathbf{q}_{i+1}$. ${}^{G}_{B}\mathbf{q}_{i}$ and ${}^{G}_{B}\mathbf{q}_{i+1}$ are the known orientations and

provided by the tracker i and $i+1$ respectively. With the known position ${}^{G}p_i$ and the segment length ${}^{S}l_{i+1}$, the position ${}^{G}p_{i+1}$ for the segment $i+1$ can be computed by

$$ {}^{G}p_{i+1} = {}^{G}p_i + {}^{G}_{B}\mathbf{q}_{i+1} \otimes {}^{S}l_{i+1} \otimes {}^{G}_{B}\mathbf{q}^{*}_{i+1} \tag{5.3} $$

where we assume the position p_0 of the joint origin is known. And the joint angle ${}^{i+1}_{i}\mathbf{q}$ in quaternion between the segment i and $i+1$ can be extracted by

$$ {}^{i+1}_{i}\mathbf{q} = {}^{G}_{B}\mathbf{q}_i \otimes {}^{G}_{B}\mathbf{q}^{*}_{i+1} \tag{5.4} $$

5.3 Attitude Estimation

We investigate the attitude estimation algorithm in this section. First of all, the filter design is explained, which actually is based on the idea of the construction of the extended Kalman filter. Following this, the filter setup is discussed, including the initial condition configuration and the noise characteristic identification of MARG.

5.3.1 Filter design

In this filter, quaternion $q = \begin{bmatrix} w, x, y, z \end{bmatrix}^T$ is employed as the representation of the orientation of the sensor, which effectively avoids the traditional problem of gimbal lock and has higher computational efficiency than other representations like Euler angles and rotation matrix. Gyroscope measures the angular rate $\omega = (\omega_x, \omega_y, \omega_z)$, with an initial known orientation, the attitude at time k can be computed by integrating over time:

$$ {}^{G}_{S}\mathbf{q}_k = \left\{ \mathbf{I}_{4\times 4} + \frac{\Delta T}{2}[\mathbf{\Omega}\times] \right\} {}^{G}_{S}\mathbf{q}_{k-1} \tag{5.5} $$

where $\mathbf{I}_{4\times 4}$ is the 4×4 identity matrix, ΔT denotes the sampling interval of the gyroscope and

$$ [\mathbf{\Omega}\times] = \begin{pmatrix} 0 & -\omega_x & -\omega_y & -\omega_z \\ \omega_x & 0 & \omega_z & -\omega_y \\ \omega_y & -\omega_z & 0 & \omega_x \\ \omega_z & \omega_y & -\omega_x & 0 \end{pmatrix} \tag{5.6} $$

This quaternion kinematic equation is employed as the process model while ${}^{G}_{S}\mathbf{q}_k$ is viewed as the hidden state of the system. For the normalised observations in the sensor frame S, ${}^{S}A = (a_x, a_y, a_z)$, ${}^{S}M = (m_x, m_y, m_z)$, from the accelerometer and magnetometer respectively, we model the observation process as

$$ \mathbf{y}_k = \begin{bmatrix} {}^{S}A & {}^{S}M \end{bmatrix}^T = \mathbf{R}({}^{G}_{S}\mathbf{q}^{*}_k) \cdot \begin{bmatrix} {}^{G}A & {}^{G}M \end{bmatrix}^T \tag{5.7} $$

where $\mathbf{R}({}^{G}_{S}\mathbf{q}^{*}_{k})$ is the rotation matrix extracted from ${}^{G}_{S}\mathbf{q}^{*}_{k}$ using the equation 5.8,

$$\mathbf{R}(\mathbf{q}) = \begin{pmatrix} w^2 + x^2 - y^2 - z^2 & 2xy - 2wz & 2wy + 2xz \\ 2wy + 2xy & w^2 - x^2 + y^2 - z^2 & 2yz - 2wx \\ 2xz - 2wy & 2yz + 2wx & w^2 - x^2 - y^2 + z^2 \end{pmatrix} \tag{5.8}$$

while ${}^{G}A$ and ${}^{G}M$ are the reference vectors and in [40] given by

$$\begin{aligned} {}^{G}A &= \begin{bmatrix} 0 & 0 & 1 \end{bmatrix} \\ {}^{G}M &= \begin{bmatrix} m_N & 0 & m_D \end{bmatrix} \\ m_D &= a_x m_x + a_y m_y + a_z m_z \\ m_N &= \sqrt{1 - m_D^2} \end{aligned} \tag{5.9}$$

Henceforth, the discrete-time nonlinear system can be rewritten as

$$\begin{aligned} \mathbf{q}_k &= \left\{ \mathbf{I}_{4\times 4} + \frac{\Delta T}{2} [\mathbf{\Omega}\times] \right\} \mathbf{q}_{k-1} + w_k, \\ \mathbf{y}_k &= \mathbf{R}(\mathbf{q}^{*}_{k}) \cdot \begin{bmatrix} {}^{G}A & {}^{G}M \end{bmatrix}^{T} + \upsilon_k \end{aligned} \tag{5.10}$$

where we use $\mathbf{q}_k$ instead of ${}^{G}_{S}\mathbf{q}_k$ for simplicity, while w_k and υ_k are the process noise and observation noise and assumed to obey white Gaussian distribution. Combing with the structure of the extended Kalman filter, the covariance $\mathbf{Q}_k$ is computed by

$$\mathbf{Q}_k = \left(\frac{\Delta T}{2} \right)^2 \mathbf{\Xi}_{k-1} \mathbf{\Sigma}_{gyro} \mathbf{\Xi}^{T}_{k-1}, \tag{5.11}$$

with the given covariance matrix $\mathbf{\Sigma}_{gyro} = \sigma_g^2 \mathbf{I}_{3\times 3}$ where σ_g denotes the deviation of angular rate. The $\mathbf{\Xi}_{k-1}$ is computed by

$$\mathbf{\Xi}_{k-1} = \begin{pmatrix} q_{1,k-1} & q_{2,k-1} & q_{3,k-1} \\ -q_{0,k-1} & q_{3,k-1} & -q_{2,k-1} \\ -q_{3,k-1} & -q_{0,k-1} & q_{1,k-1} \\ q_{2,k-1} & -q_{1,k-1} & -q_{0,k-1} \end{pmatrix}. \tag{5.12}$$

In contrast, the covariance $\mathbf{R}_k$ for the observation noise is simply equal to the diagonal matrix of the covariance of the accelerometer and magnetometer.

$$\mathbf{R}_k = diag(\mathbf{R}_{1,k}, \mathbf{R}_{2,k}) \tag{5.13}$$

where $\mathbf{R}_{1,k} = \sigma_a^2 \mathbf{I}_{3\times3}$ and $\mathbf{R}_{2,k} = \sigma_m^2 \mathbf{I}_{3\times3}$. As well, the observation matrices $\mathbf{H}_k$ is defined to be the following Jacobians

$$\mathbf{H}_k = \begin{pmatrix} \mathbf{H}_{1,k} \\ \mathbf{H}_{2,k}) \end{pmatrix} \tag{5.14}$$

where

$$\mathbf{H}_{1,k} = 2 \begin{pmatrix} -\mathbf{q}_{y,k}^- & \mathbf{q}_{z,k}^- & -\mathbf{q}_{w,k}^- & \mathbf{q}_{x,k}^- \\ \mathbf{q}_{x,k}^- & \mathbf{q}_{w,k}^- & \mathbf{q}_{z,k}^- & \mathbf{q}_{y,k}^- \\ \mathbf{q}_{w,k}^- & -\mathbf{q}_{x,k}^- & -\mathbf{q}_{y,k}^- & \mathbf{q}_{z,k}^- \end{pmatrix} \tag{5.15}$$

and $\mathbf{H}_{2,k}$ is defined by the formula

$$\mathbf{H}_{2,k} = 2 \begin{pmatrix} h_{0,0} & h_{0,1} & h_{0,2} & h_{0,3} \\ h_{1,0} & h_{1,1} & h_{1,2} & h_{1,3} \\ h_{2,0} & h_{2,1} & h_{2,2} & h_{2,3} \end{pmatrix} \tag{5.16}$$

where

$$\begin{aligned} h_{0,0} &= \mathbf{q}_{w,k}^- m_N - \mathbf{q}_{y,k}^- m_D & h_{0,1} &= \mathbf{q}_{x,k}^- m_N + \mathbf{q}_{z,k}^- m_D \\ h_{0,2} &= \mathbf{q}_{y,k}^- m_N - \mathbf{q}_{w,k}^- m_D & h_{0,3} &= -\mathbf{q}_{z,k}^- m_N - \mathbf{q}_{x,k}^- m_D \\ h_{1,0} &= -\mathbf{q}_{z,k}^- m_N + \mathbf{q}_{x,k}^- m_D & h_{1,1} &= \mathbf{q}_{y,k}^- m_N + \mathbf{q}_{w,k}^- m_D \\ h_{1,2} &= \mathbf{q}_{x,k}^- m_N + \mathbf{q}_{z,k}^- m_D & h_{1,3} &= \mathbf{q}_{w,k}^- m_N + \mathbf{q}_{y,k}^- m_D \\ h_{2,0} &= \mathbf{q}_{y,k}^- m_N + \mathbf{q}_{w,k}^- m_D & h_{2,1} &= \mathbf{q}_{z,k}^- m_N - \mathbf{q}_{x,k}^- m_D \\ h_{2,2} &= \mathbf{q}_{w,k}^- m_N - \mathbf{q}_{y,k}^- m_D & h_{2,3} &= \mathbf{q}_{x,k}^- m_N + \mathbf{q}_{z,k}^- m_D \end{aligned} \tag{5.17}$$

In general, the maximum fusion rate of the Kalman filter is limited by the lowest sampling rate of the utilized sensors. For example, in modern sensors, gyroscope and accelerometer have the same high sampling rate usually, while magnetometer outputs the measurement in relative low rate. Such limitation is a waste of the performance of the sensor that can senses the signal in high sampling rate, which degrades overall performance of the application. Thus, the designed filter adopts a multi-rate filter architecture. With this architecture, this filter allows the sensors to work at an asynchronous sample rate and takes full advantage of the performance of all the sensors. The workflow of this filter is summarized as the following:

(1) Predict the state if the gyroscope is available: $\mathbf{q}_k^- = \left\{\mathbf{I}_{4\times4} + \frac{\Delta T}{2}[\mathbf{\Omega}\times]\right\} \mathbf{q}_{k-1}$.

(2) Covariance prediction: $\mathbf{P}_k^- = \mathbf{F}_k \mathbf{P}_{k-1} \mathbf{F}_k^T + \mathbf{Q}_k$ with $\mathbf{F}_k = \left\{\mathbf{I}_{4\times4} + \frac{\Delta T}{2}[\mathbf{\Omega}\times]\right\}$.

(3) If the accelerometer and magnetometer are both available, execute the missions of this block and move to step (5), if only accelerometer available, move to step (4).

i Observations: $\mathbf{y}_k = \begin{bmatrix} {}^S A & {}^S M \end{bmatrix}^T$.

ii Kalman gain: $\mathbf{K} = \mathbf{P}_k^- \mathbf{H}_k^T (\mathbf{H}_k \mathbf{P}_k^- \mathbf{H}_k^T + \mathbf{R}_k)^{-1}$.

iii Correct the state: $\mathbf{q}_k = \mathbf{q}_k^- + \mathbf{K}(\mathbf{y}_k - \mathbf{y}_k^-)$.

iv Update the covariance: $\mathbf{P}_k = (\mathbf{I}_{4\times 4} - \mathbf{K})\mathbf{P}_k^-$.

(4) Correct the quaternion with the readings from the accelerometer:

i Observations: $\mathbf{y}_k = \begin{bmatrix} {}^S A \end{bmatrix}^T$.

ii Kalman gain: $\mathbf{K} = \mathbf{P}_k^- \mathbf{H}_{1,k}^T (\mathbf{H}_{1,k} \mathbf{P}_k^- \mathbf{H}_{1,k}^T + \mathbf{R}_{1,k})^{-1}$.

iii Correct the state: $\mathbf{q}_k = \mathbf{q}_k^- + \mathbf{K}(\mathbf{y}_k - \mathbf{y}_k^-)$.

iv Update the covariance: $\mathbf{P}_k = (\mathbf{I}_{4\times 4} - \mathbf{K})\mathbf{P}_k^-$.

(5) Update the state and covariance for the next turn and move to step (1): $\mathbf{q}_{k-1} = \mathbf{q}_k$, $\mathbf{P}_{k-1} = \mathbf{P}_k$

5.3.2 Filter setup

When deploying the designed filter to the tracker, the initial conditions are set to $\mathbf{q}_0 = \begin{bmatrix} 1 & 0 & 0 & 0 \end{bmatrix}^T$ and $\mathbf{P}_0 = 0.001 \cdot \mathbf{I}_{4\times 4}$. When powering up, the tracker always requires several minutes for warming up before conducting any motion capture activities. Also, to obtain better dynamic performance, the fusion of the gyroscope and accelerometer are running at 200 Hz, while the magnetometer is fused at the rate of 100 Hz because of the limitation of the maximum sampling rate of the magnetometer. The output rate of the estimated attitude is subjected to the settings of the timer of the microcontroller.

In addition, correct configurations of the sensor noise characteristics are conductive to achieve optimum performance of the filter. Normally, the standard approach of characterization of noise for MARG sensors is Allan variance and its square-root, Allan deviation, which is introduced in [84]. It is defined as a function of inter sample distance τ, where x_n denotes the time series of phase observations with length N and spaced by the measurement interval τ:

$$\sigma^2(\tau) = \frac{1}{2(N-2)\tau^2} \sum_{n=1}^{N-2} (x_{n+2} - 2x_{n+1} + x_n)^2 \tag{5.18}$$

Several types of noise can be identified by fitting the computed Allan deviation and the cluster time τ. In this paper, only the white noises, σ_g for the gyroscope, σ_a for the accelerometer and σ_m for the magnetometer, are considered, which can be recognized by observing the value at $\tau = 1$ in the log-log plot of Allan deviation and the cluster time τ. The analysis results will be described in the experiment section.

5.4 Experiments and Results

In this section, several experiments are conducted and the results are discussed. Results of Allan variance are shown in the first subsection. The second subsection evaluates the performance of the attitude estimation of the motion tracker by comparing with the reference measurement provided by the optical system, namely Vicon. Thirdly, the assessment of time synchronization of the motion trackers is carried out. At last, with the synchronized motion trackers, the built motion capture system is validated during human walking. All the experiments are carried out with 100 Hz sampling rate, the measurement range of ± 2 g for accelerometer and $\pm 2000\,^{\circ}/s$ for gyroscope and the low pass filter is set to 98 Hz.

5.4.1 Results of Allan variance

To obtain the Allan variance, the tested tracker is placed on the foam board, which plays the role of a filter to damp the vibrations from the surrounding environment. Moreover, all the metal objects that could cause the distortion of the magnetic field are cleared. We record the measurements over 4 hours.

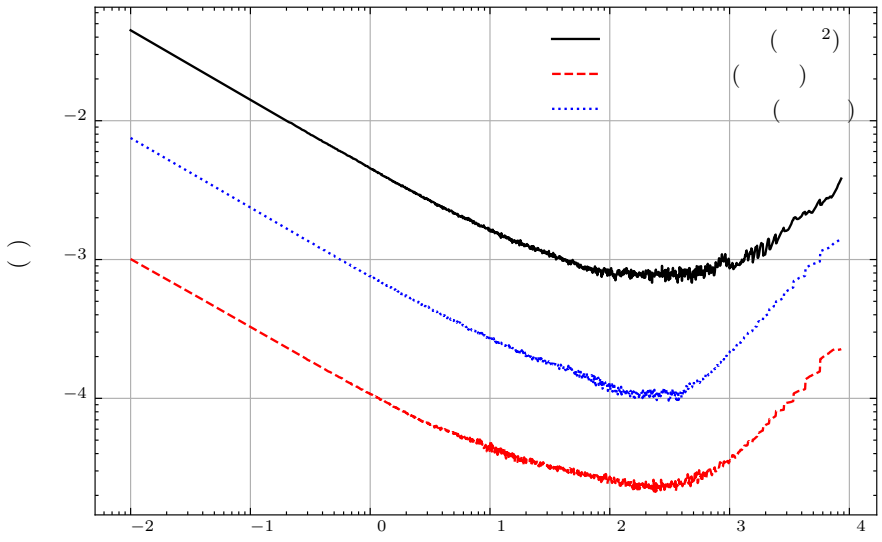

Figure 5.4: Allan Deviation of the Tested Motion Tracker

Fig. 5.4 shows the analysis results of the Allan variances of the three sensors. According to this graph, the white noise of the three sensors can be easily identified and Table. 5.2 lists the results. The results of noise identification will be utilized to setup the attitude estimation filter.

Table 5.2: Results of Noise Identification

	Gyroscope	Accelerometer	Magnetometer
σ	0.000165 rad/s	0.007034 m/s^2	0.000825 $Gauss$

5.4.2 Accuracy of the attitude estimation

In this section, we evaluate the performance of the attitude estimation with Vicon, which is an optical system that consists of eight infrared cameras and is able to track the position of optical markers continually. When attaching three non co-linear markers to the rigid body, the orientation of which can be extracted from the three measured positions and viewed as the reference orientation. Fig. 5.5 shows the experimental device. We first keep the device stationary and align the two coordinate system of the sensor and Vicon using cubature Kalman filter [23]. Further, the experimental data is acquired from the random motion generated by moving the tacker manually. Similar with the method to synchronize the trackers, time synchronization between the tracker and Vicon is done by locating the maximum value of the correlation rate of the angular rate from the two system.

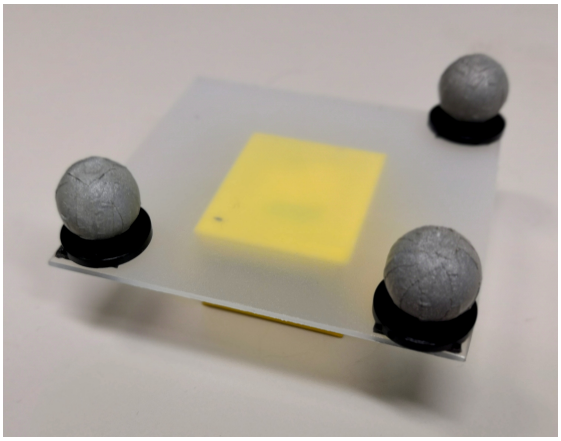

Figure 5.5: TExperimental Device for Attitude Estimation Evaluation

Table. 5.3 shows the RMSE of three trials. Although the magnetometer is calibrated using the ellipsoid fitting algorithm [55], the angle of yaw still behaves badly, there are two probable factors that cause this; the first is taht the iron house, the experiment room of Vicon, could disturb the magnetic field, and the second is that the magnetometer could suffer from low performance. In practical, the magnetometer can be discarded by increasing σ_m to infinity when it performs poorly. In contrast, angles of pitch and roll have relative reliable performance.

Table 5.3: RMSE [in deg] for Attitude Estimation

Trials	Roll	Pitch	Yaw
0	1.52	2.03	14.30
1	1.38	0.64	14.12
2	1.23	1.96	14.89

5.4.3 Time synchronization assessment

As mentioned before, time synchronization of the trackers is done by the consistency of the gyroscopes under the same condition. Although there is a positive correlation between the accuracy of time synchronization and the sampling rate of the gyroscope, and the error of time synchronization should be less than or equal to one sampling interval of the gyroscope theoretically, it's still essential to investigate the feasibility and the stability over time.

In this experiment, four trackers are mounted on the wooden rigid segment. We choose the tracker 4 as the benchmark and collect the static data to find other trackers to the tracker 4 alignment. Then we move the experimental device randomly and the progress lasts for one hour approximately. For data analysis, the vector length for performing cross-correlation is investigated in order to obtain the accurate time offset, which also determines how long for time synchronization. On the other hand, the stability of time synchronization over time is analyzed by comparing the calculated time offset at different times.

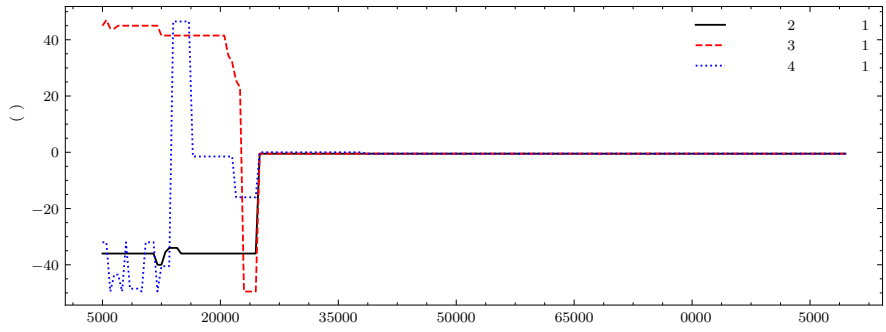

Figure 5.6: Vector Length Versus Calculated Time Offset

The analysis results are shown in Fig. 5.6 and Fig. 5.7. From Fig. 5.6, we can conclude that the offset is stable when the vector length is larger than 40000. This is to say, we need more than 6 minutes data for time synchronization at least. Although it adds the complexity of the implementation of devices in some way, it may be acceptable for application without strict time limitations. Fig. 5.7 shows that the time offset is changed with the increasing of working time, this probably because the clock precision of sensors is different. Even so, the changing of time offset can be ignored for short time monitoring.

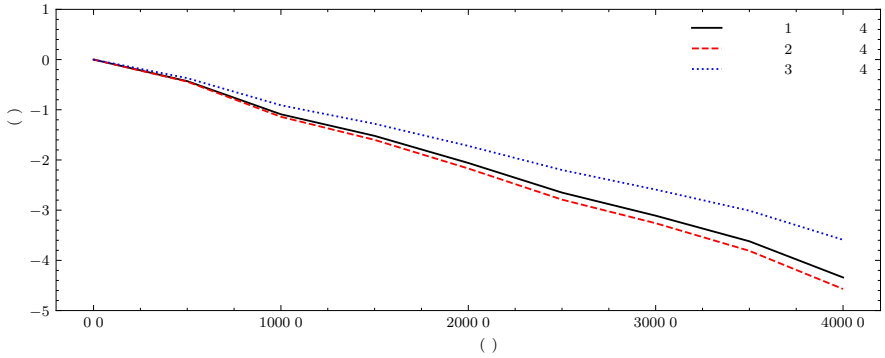

Figure 5.7: Working Time Versus Time Offset

5.4.4 Validation during walking

With synchronized trackers, the feasibility of the built motion capture system is validated during walking in this experiment. The trackers are fixed on human body, as Fig. 5.11 suggests, they are distributed on waist, thigh, calf and instep respectively. In the same way, this experiment is conducted with Vicon and all the trackers are equipped with three optical markers. We extract the joint angle from both of trackers' data and Vicon's data and employ RMSE as the evaluation metrics. And, the magnetometer is discarded by increasing σ_m due to the magnetic disturbance.

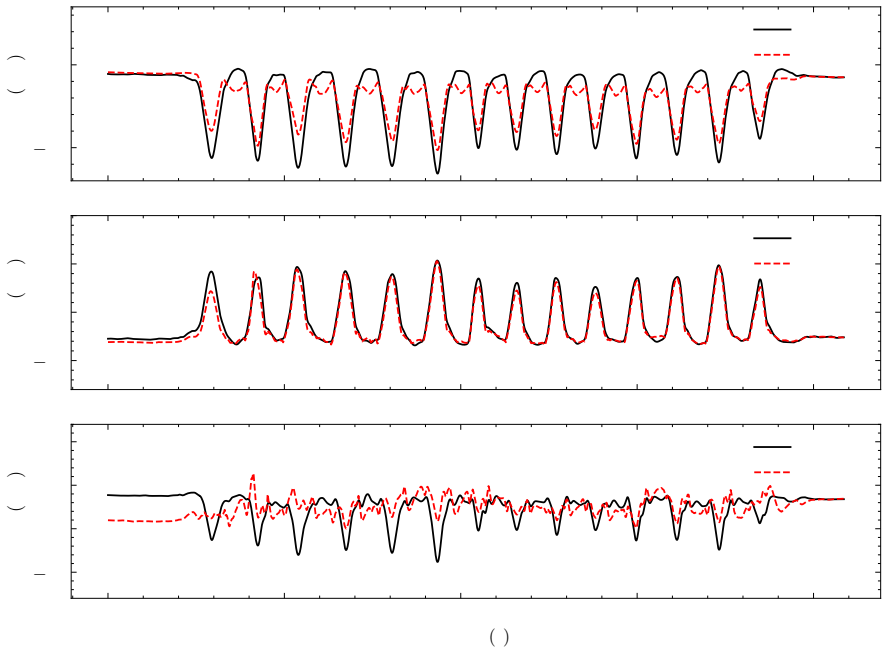

Figure 5.8: Hip: Joint Angle between Waist and Thigh

Fig. 5.8, Fig. 5.9 and Fig. 5.10 depicts the analyzed results where the joint angle is represented using euler angle for intuition. Evidently, there is a good consistency between the tackers and Vicon, except the angle of yaw performed below other two. In Fig. 5.10, as a result of our analysis, the anomaly in the beginning is caused by the

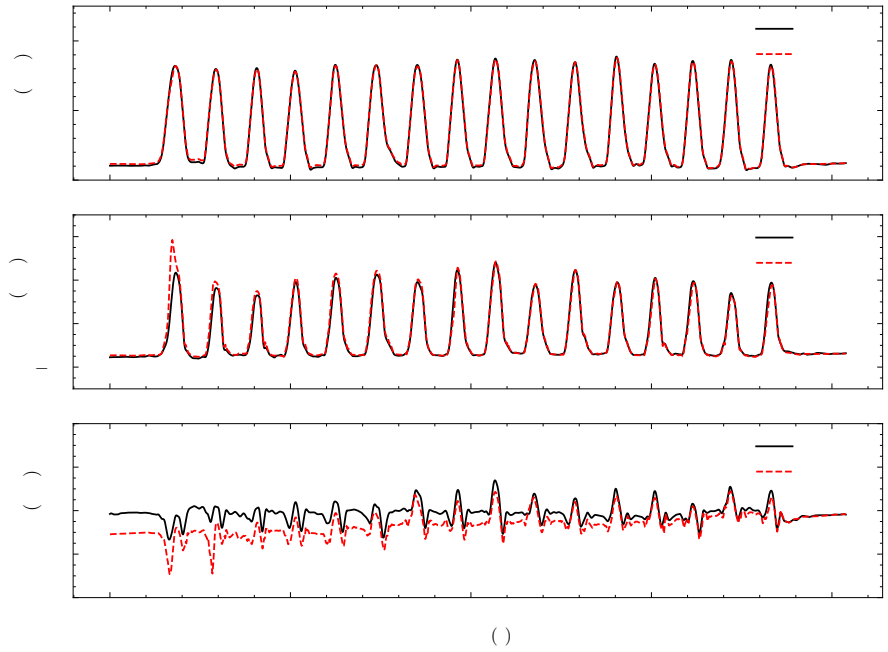

Figure 5.9: Knee: Joint Angle between Thigh and Calf

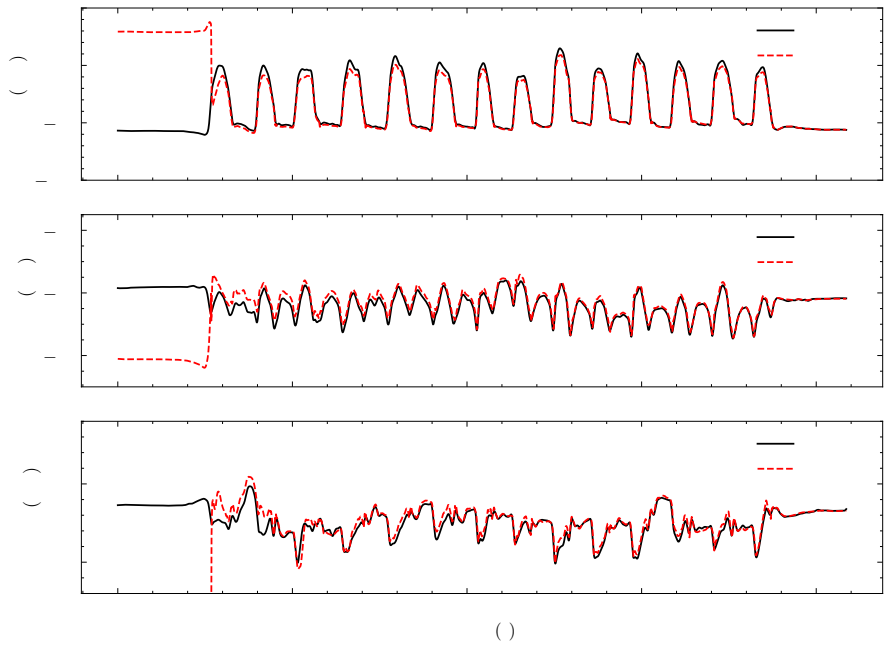

Figure 5.10: Ankle: Joint Angle between Calf and Foot

sudden lifting of the foot and this part is excluded when calculating RMSE. Table. 5.4 shows the calculated RMSE for two trials.

In this experiment, we investigate the feasibility of the built motion capture system by evaluating the accuracy of estimated joint angles. Although the angle of yaw of the trackers is without correction of the magnetometer and its inaccuracy could affect the accuracy of the extracted joint angle, the experimental results still reflect the good consistency between the proposed trackers and the optical system.

(a) View from Back

(b) View from Right

(c) Walking

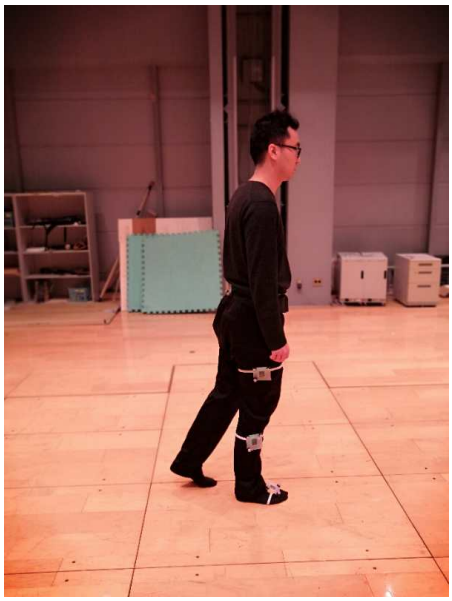

(d) Walking

Figure 5.11: Motion Tracking during Walking

Table 5.4: RMSE [in deg] of Joint Angles

		RMSE		
Trials	Joint Angle	Roll	Pitch	Yaw
0	Hip	7.99	2.68	9.18
	Knee	0.72	2.80	5.63
	Ankle	2.94	1.22	2.67
1	Hip	7.79	3.90	10.25
	Knee	1.14	2.37	6.25
	Ankle	2.52	2.21	5.09

5.5 Summary

In this chapter, novel wireless time synchronized motion trackers are presented. First of all, we introduced the work principles of the proposed motion tracker. This part explained the architecture of the motion tracker, the workflow of the residing program and the establishment of motion capture system. The tracker is compact and easy to use. In particular, the scalability of the sensor network is not limited and a low-cost and easy-to-operate method is proposed for time synchronization of the trackers. And, segment kinematics are briefly introduced, which includes the step for system calibration and the update of the position of the joint. Then, quaternion-based EKF to multi-rate sensor fusion is designed for the attitude estimation, this filter enables the sensors working at an asynchronous measurement rate and takes full advantage of the performance of the sensors. Moreover, the setup of the filter is described particularly the Allan variance is introduced and utilized in order to achieve optimum performance.

With the proposed trackers, several experiments are carried out. At first, the white noise of the sensors are identified using Allan variance and utilized to setup the parameters of the filter. Then the accuracy of the attitude estimation is assessed with the reference measurements provided by Vicon. Results indicate that angles of pitch and roll provides reliable performance, while the angle of yaw suffers from the magnetic disturbance or the low performance of the magnetometer. Further, the feasibility and stability of time synchronization is investigated. Results shows that, it needs more 6 minutes for time synchronization and is acceptable for application without strict time limitations, and time synchronization is stable within a short time. Finally, to verify the feasibility of the trackers for motion capture, we validate the established motion capture system during human walking. Although the accuracy of the joint angle suffers from the inaccuracy of the angle of yaw, the experiment results still reflect that there is a good consistency between the proposed trackers and the optical system.

Chapter 6

Conclusion

In this chapter, we conclude the dissertation by summarizing the conclusions of Chapter 3, 4 and 5.

In Chapter 3, we derive a simplified measurement model from TRIAD method and establish the LEKF for MARG sensors attitude estimation. In this filter, the quaternion kinematic equation is simply adopted as the process model, and the simplified measurement model is utilized to process acceleration and magnetic field observations. In consequence of the simplified observation model, up to half of parameters of Jacobian matrix are constant and only a few amount of computation is necessary for other parameters of Jacobian, which are similar and have the common factors. This significantly reduces the computational efforts.

Experiments are carried out with a commercial sensor for data collection and an optical system to provide the reference angles. The performance of the proposed filter for human motion capture and UAV applications are evaluated separately. Results indicate that, for both application scenarios, the proposed filter performs well, particularly the evaluation during the flight on an UAV shows that the proposed filter is robust. On the other hand, the comparisons between the proposed filter and the representative filters prove that the proposed filter is faster and its accuracy is improved in some way.

In Chapter 4, a matrix operation accelerator is proposed to accelerate SPKF for real-time orientation estimation. These advanced filters have higher performance in terms of accuracy and more robust than EKF. It's quite essential for modern applications particularly in hash environment. The accelerator is programmed in C and synthesized using Xilinx's Vivado Design Suite. We conduct the experiment on Zynq-7020 (XC7Z020-1CLG484). The experimental results show that the accelerator is efficient of the computation and saves silicon. With this, on one hand, it not only improves the performance but also offloads the heavy computation from the CPU. On the other hand, it's reusable to speedup other matrix operation based algorithms, which will save time for redesign. Although some of computation of SPKF is executed in software and can not be solved as the matrix operation, the proposed scheme is still a considerable

solution to the problem of algorithm acceleration.

In Chapter 5, novel wireless time synchronized motion trackers are presented. First of all, we introduced the work principles of the proposed motion tracker. This part explained the architecture of the motion tracker, the workflow of the residing program and the establishment of motion capture system. The tracker is compact and easy to use. In particular, the scalability of the sensor network is not limited and a low-cost and easy-to-operate method is proposed for time synchronization of the trackers. And, segment kinematics are briefly introduced, which includes the step for system calibration and the update of the position of the joint. Then, quaternion-based EKF to multi-rate sensor fusion is designed for the attitude estimation, this filter enables the sensors working at an asynchronous measurement rate and takes full advantage of the performance of the sensors. Moreover, the setup of the filter is described particularly the Allan variance is introduced and utilized in order to achieve optimum performance.

With the proposed trackers, several experiments are carried out. At first, the white noise of the sensors are identified using Allan variance and utilized to setup the parameters of the filter. Then the accuracy of the attitude estimation is assessed with the reference measurements provided by Vicon. Results indicate that angles of pitch and roll provides reliable performance, while the angle of yaw suffers from the magnetic disturbance or the low performance of the magnetometer. Further, the feasibility and stability of time synchronization is investigated. Results shows that, it needs more 6 minutes for time synchronization and is acceptable for application without strict time limitations, and time synchronization is stable within a short time. Finally, to verify the feasibility of the trackers for motion capture, we validate the established motion capture system during human walking. Although the accuracy of the joint angle suffers from the inaccuracy of the angle of yaw, the experiment results still reflect that there is a good consistency between the proposed trackers and the optical system.

Acknowledgment

I wish to express my sincere appreciation to my supervisor, Prof. Lei Jing, for the patient guidance, encouragement and advice he has provided throughout my time as his student. I have been extremely lucky to have a supervisor who cared so much about my life and work, who responded to my questions and queries so promptly and modestly, and who found the opportunity of the internship for me and accompanied me for almost five years.

I also would like to thank the constructive comments and suggestions from the review committee members; Prof. Xiang Li, Prof. Kazuyoshi Mori and Prof. Keitaro Naruse. Their professional opinions have significantly improved my dissertation. As well, I sincerely thanks their time and attention on my research topic. Through the defending of the dissertation, I learned a lot.

The assistance from laboratory secretary, Mrs. Hoshi; Dr. Huakun Huang, Mr. Chenghong Lu and all other members of our laboratory is truly appreciated. Mrs. Hoshi often helped me borrow the experiment room and cared my daily life in the Lab. Dr. Huang always shared experience and considerations on research with me. And Mr. Lu usually assisted me to complete the experiments. Without their support, this research could not have reached its goal.

Finally, I wish to acknowledge the support and great love of my family, my girlfriend, Huicong Yu; my father, Xinzhong Dai; and my grandfather, Jiayun Dai. They kept me going on and this work would not have been possible without their input.

Sincerely thanks you all. Best wishes to you!

References

[1] I. Board, "Ieee standard specification format guide and test procedure for single-axis interferometric fiber optic gyros," *IEEE Std*, pp. 952–1997, 1998.

[2] Y.-B. Jia, "Quaternions and rotations," *Com S*, vol. 477, no. 577, p. 15, 2008.

[3] B. Kenwright, "A beginners guide to dual-quaternions: what they are, how they work, and how to use them for 3d character hierarchies," 2012.

[4] H. Harrison, "Quaternions and rotation sequences: a primer with applications to orbits, aerospace and virtual reality, jb kuipers, princeton university press, 41 william street, princeton, nj 08540, usa. 1999. 372pp. illustrated.£ 35.00. isbn 0-691-05872-5." *The Aeronautical Journal*, vol. 103, no. 1021, pp. 175–175, 1999.

[5] S. W. Shepperd, "Quaternion from rotation matrix," *Journal of Guidance and Control*, vol. 1, no. 3, pp. 223–224, 1978.

[6] S. Sarabandi and F. Thomas, "Accurate computation of quaternions from rotation matrices," in *International Symposium on Advances in Robot Kinematics*. Springer, 2018, pp. 39–46.

[7] Z.-Q. Zhang, "Two-step calibration methods for miniature inertial and magnetic sensor units," *IEEE Transactions on Industrial Electronics*, vol. 62, no. 6, pp. 3714–3723, 2014.

[8] G. Wahba, "A least squares estimate of satellite attitude," *SIAM review*, vol. 7, no. 3, pp. 409–409, 1965.

[9] J. R. Wertz, *Spacecraft attitude determination and control*. Springer Science & Business Media, 2012, vol. 73.

[10] F. L. Markley, "Attitude determination using vector observations: A fast optimal matrix algorithm," 1993.

[11] J. Keat, "Analysis of least-squares attitude determination routine doaop," Technical Report CSC/TM-77/6034, Comp. Sc. Corp, Tech. Rep., 1977.

[12] M. D. Shuster and S. D. Oh, "Three-axis attitude determination from vector observations," *Journal of guidance and Control*, vol. 4, no. 1, pp. 70–77, 1981.

[13] D. Mortari, "Esoq: A closed-form solution to the wahba problem," *Journal of the Astronautical Sciences*, vol. 45, no. 2, pp. 195–204, 1997.

[14] ——, "Second estimator of the optimal quaternion," *Journal of Guidance, Control, and Dynamics*, vol. 23, no. 5, pp. 885–888, 2000.

[15] F. L. Markley and D. Mortari, "Quaternion attitude estimation using vector observations." *Journal of the Astronautical Sciences*, vol. 48, no. 2, pp. 359–380, 2000.

[16] J. Wu, Z. Zhou, B. Gao, R. Li, Y. Cheng, and H. Fourati, "Fast linear quaternion attitude estimator using vector observations," *IEEE Transactions on Automation Science and Engineering*, vol. 15, no. 1, pp. 307–319, 2017.

[17] F. L. Markley and J. L. Crassidis, *Fundamentals of spacecraft attitude determination and control*. Springer, 2014, vol. 33.

[18] E. Foxlin, "Inertial head-tracker sensor fusion by a complementary separate-bias kalman filter," 1996.

[19] S. Madgwick, "An efficient orientation filter for inertial and inertial/magnetic sensor arrays," *Report x-io and University of Bristol (UK)*, vol. 25, pp. 113–118, 2010.

[20] S. J. Julier and J. K. Uhlmann, "Unscented filtering and nonlinear estimation," *Proceedings of the IEEE*, vol. 92, no. 3, pp. 401–422, 2004.

[21] M. NøRgaard, N. K. Poulsen, and O. Ravn, "New developments in state estimation for nonlinear systems," *Automatica*, vol. 36, no. 11, pp. 1627–1638, 2000.

[22] K. Ito, "Gaussian filter for nonlinear filtering problems," in *Proceedings of the 39th IEEE Conference on Decision and Control (Cat. No. 00CH37187)*, vol. 2. IEEE, 2000, pp. 1218–1223.

[23] I. Arasaratnam and S. Haykin, "Cubature kalman filters," *IEEE Transactions on automatic control*, vol. 54, no. 6, pp. 1254–1269, 2009.

[24] D. Roetenberg, H. Luinge, and P. Slycke, "Xsens mvn: Full 6dof human motion tracking using miniature inertial sensors," *Xsens Motion Technologies BV, Tech. Rep*, vol. 1, 2009.

[25] R. E. Kalman, "A new approach to linear filtering and prediction problems," 1960.

[26] G. Welch, G. Bishop *et al.*, "An introduction to the kalman filter," 1995.

[27] G. Bishop, G. Welch *et al.*, "An introduction to the kalman filter," *Proc of SIGGRAPH, Course*, vol. 8, no. 27599-23175, p. 41, 2001.

[28] S. M. Kay, *Fundamentals of statistical signal processing*. Prentice Hall PTR, 1993.

[29] M. I. Ribeiro, "Kalman and extended kalman filters: Concept, derivation and properties," *Institute for Systems and Robotics*, vol. 43, 2004.

[30] G. A. Terejanu *et al.*, "Extended kalman filter tutorial," *University at Buffalo*, 2008.

[31] A. Hussen and I. Jleta, "Low cost inertial sensors modeling using allan variance," *International Journal of Computer, Electrical, Automation, Control and Information Engineering*, vol. 9, no. 5, pp. 1237–1242, 2015.

[32] M. Matejček and M. Šostronek, "Computation and evaluation allan variance results," in *2016 New Trends in Signal Processing (NTSP)*. IEEE, 2016, pp. 1–9.

[33] R. J. Vaccaro and A. S. Zaki, "Statistical modeling of rate gyros," *IEEE Transactions on Instrumentation and Measurement*, vol. 61, no. 3, pp. 673–684, 2011.

[34] B. IEEE, "Ieee standard specification format guide and test procedure for single-axis interferometric fiber optic gyros," 1998.

[35] H. G. De Marina, F. J. Pereda, J. M. Giron-Sierra, and F. Espinosa, "Uav attitude estimation using unscented kalman filter and triad," *IEEE Transactions on Industrial Electronics*, vol. 59, no. 11, pp. 4465–4474, 2011.

[36] H. G. de Marina, F. Espinosa, and C. Santos, "Adaptive uav attitude estimation employing unscented kalman filter, foam and low-cost mems sensors," *Sensors*, vol. 12, no. 7, pp. 9566–9585, 2012.

[37] G. Bellusci, F. Dijkstra, and P. Slycke, "Xsens mtw: Miniature wireless inertial motion tracker for highly accurate 3d kinematic applications," *Xsens Technologies*, 2013.

[38] X. Meng, Z.-Q. Zhang, J.-K. Wu, W.-C. Wong, and H. Yu, "Self-contained pedestrian tracking during normal walking using an inertial/magnetic sensor module," *IEEE Transactions on Biomedical Engineering*, vol. 61, no. 3, pp. 892–899, 2013.

[39] S. O. Madgwick, A. J. Harrison, and R. Vaidyanathan, "Estimation of imu and marg orientation using a gradient descent algorithm," in *2011 IEEE international conference on rehabilitation robotics*. IEEE, 2011, pp. 1–7.

[40] J. Wu, Z. Zhou, J. Chen, H. Fourati, and R. Li, "Fast complementary filter for attitude estimation using low-cost marg sensors," *IEEE Sensors Journal*, vol. 16, no. 18, pp. 6997–7007, 2016.

[41] J. Wu, Z. Zhou, H. Fourati, R. Li, and M. Liu, "Generalized linear quaternion complementary filter for attitude estimation from multisensor observations: An optimization approach," *IEEE Transactions on Automation Science and Engineering*, 2019.

[42] N. Trawny and S. I. Roumeliotis, "Indirect kalman filter for 3d attitude estimation," *University of Minnesota, Dept. of Comp. Sci. & Eng., Tech. Rep*, vol. 2, p. 2005, 2005.

[43] A. M. Sabatini, "Quaternion-based extended kalman filter for determining orientation by inertial and magnetic sensing," *IEEE Transactions on Biomedical Engineering*, vol. 53, no. 7, pp. 1346–1356, 2006.

[44] R. G. Valenti, I. Dryanovski, and J. Xiao, "A linear kalman filter for marg orientation estimation using the algebraic quaternion algorithm," *IEEE Transactions on Instrumentation and Measurement*, vol. 65, no. 2, pp. 467–481, 2015.

[45] W. Li and J. Wang, "Magnetic sensors for navigation applications: an overview," *The Journal of navigation*, vol. 67, no. 2, pp. 263–275, 2014.

[46] J. L. Marins, X. Yun, E. R. Bachmann, R. B. McGhee, and M. J. Zyda, "An extended kalman filter for quaternion-based orientation estimation using marg sensors," in *Proceedings 2001 IEEE/RSJ International Conference on Intelligent Robots and Systems. Expanding the Societal Role of Robotics in the the Next Millennium (Cat. No. 01CH37180)*, vol. 4. IEEE, 2001, pp. 2003–2011.

[47] H. Fourati, N. Manamanni, L. Afilal, and Y. Handrich, "Complementary observer for body segments motion capturing by inertial and magnetic sensors," *IEEE/ASME transactions on Mechatronics*, vol. 19, no. 1, pp. 149–157, 2012.

[48] H. D. Black, "A passive system for determining the attitude of a satellite," *AIAA journal*, vol. 2, no. 7, pp. 1350–1351, 1964.

[49] ——, "Early development of transit, the navy navigation satellite system," *Journal of Guidance, Control, and Dynamics*, vol. 13, no. 4, pp. 577–585, 1990.

[50] W.-Y. Loh and Y.-S. Shih, "Split selection methods for classification trees," *Statistica sinica*, pp. 815–840, 1997.

[51] M. Euston, P. Coote, R. Mahony, J. Kim, and T. Hamel, "A complementary filter for attitude estimation of a fixed-wing uav," in *2008 IEEE/RSJ International Conference on Intelligent Robots and Systems*. IEEE, 2008, pp. 340–345.

[52] S. Guo, J. Wu, Z. Wang, and J. Qian, "Novel marg-sensor orientation estimation algorithm using fast kalman filter," *Journal of Sensors*, vol. 2017, 2017.

[53] O. Särkkä, T. Nieminen, S. Suuriniemi, and L. Kettunen, "A multi-position calibration method for consumer-grade accelerometers, gyroscopes, and magnetometers to field conditions," *IEEE Sensors Journal*, vol. 17, no. 11, pp. 3470–3481, 2017.

[54] Z. Yang, S. Yan, and B. Li, "Hybrid calibration method for three-axis gradiometer," *IEEE Magnetics Letters*, vol. 8, pp. 1–5, 2017.

[55] J. Fang, H. Sun, J. Cao, X. Zhang, and Y. Tao, "A novel calibration method of magnetic compass based on ellipsoid fitting," *IEEE Transactions on Instrumentation and Measurement*, vol. 60, no. 6, pp. 2053–2061, 2011.

[56] R. G. Valenti, I. Dryanovski, and J. Xiao, "A linear kalman filter for marg orientation estimation using the algebraic quaternion algorithm," *IEEE Transactions on Instrumentation and Measurement*, vol. 65, no. 2, pp. 467–481, 2016.

[57] J.-m. Duan, D. Liu, H.-x. Yu, and H. Shi, "An improved fastslam algorithm for autonomous vehicle based on the strong tracking square root central difference kalman filter," in *2015 IEEE 18th International Conference on Intelligent Transportation Systems*. IEEE, 2015, pp. 693–698.

[58] D. Liu, J. Duan, and H. Shi, "A strong tracking square root central difference fastslam for unmanned intelligent vehicle with adaptive partial systematic resampling," *IEEE Transactions on Intelligent Transportation Systems*, vol. 17, no. 11, pp. 3110–3120, 2016.

[59] H. ANKIŞHAN, F. Ari, E. Ö. TARTAN, and A. G. PAKFİLİZ, "Square root central difference-based fastslam approach improved by differential evolution," *Turkish Journal of Electrical Engineering & Computer Sciences*, vol. 24, no. 3, pp. 994–1013, 2016.

[60] S. J. Julier and J. K. Uhlmann, "New extension of the kalman filter to nonlinear systems," in *Signal processing, sensor fusion, and target recognition VI*, vol. 3068. International Society for Optics and Photonics, 1997, pp. 182–194.

[61] V. Bonato, R. Peron, D. F. Wolf, J. A. de Holanda, E. Marques, and J. M. Cardoso, "An fpga implementation for a kalman filter with application to mobile robotics,"

in *2007 International Symposium on Industrial Embedded Systems*. IEEE, 2007, pp. 148–155.

[62] D. T. Tertei, J. Piat, and M. Devy, "Fpga design and implementation of a matrix multiplier based accelerator for 3d ekf slam," in *2014 International Conference on ReConFigurable Computing and FPGAs (ReConFig14)*. IEEE, 2014, pp. 1–6.

[63] J. Soh and X. Wu, "An fpga-based unscented kalman filter for system-on-chip applications," *IEEE Transactions on Circuits and Systems II: Express Briefs*, vol. 64, no. 4, pp. 447–451, 2017.

[64] S. Mie, Y. Okuyama, Y. Sato, Y. Chan, N. K. Dang, and B. A. Abderazek, "Real-time uav attitude heading reference system using extended kalman filter for programmable soc," in *2017 IEEE 11th International Symposium on Embedded Multicore/Many-core Systems-on-Chip (MCSoC)*. IEEE, 2017, pp. 136–142.

[65] E. A. Wan and R. Van Der Merwe, "The unscented kalman filter," *Kalman filtering and neural networks*, pp. 221–280, 2001.

[66] R. Van Der Merwe *et al.*, "Sigma-point kalman filters for probabilistic inference in dynamic state-space models," Ph.D. dissertation, OGI School of Science & Engineering at OHSU, 2004.

[67] K. Papadimitriou, A. Dollas, and S. Hauck, "Performance of partial reconfiguration in fpga systems: A survey and a cost model," *ACM Transactions on Reconfigurable Technology and Systems (TRETS)*, vol. 4, no. 4, p. 36, 2011.

[68] C. Bregler, "Motion capture technology for entertainment [in the spotlight]," *IEEE Signal Processing Magazine*, vol. 24, no. 6, pp. 160–158, 2007.

[69] D. Šimšík, J. Karchňák, B. Jobbágy, and A. Galajdová, "Design of inertial module for rehabilitation device," in *2013 IEEE 11th International Symposium on Applied Machine Intelligence and Informatics (SAMI)*. IEEE, 2013, pp. 33–36.

[70] O. M. Giggins, K. T. Sweeney, and B. Caulfield, "Rehabilitation exercise assessment using inertial sensors: a cross-sectional analytical study," *Journal of neuroengineering and rehabilitation*, vol. 11, no. 1, p. 158, 2014.

[71] L. Jing, Y. Zhou, Z. Cheng, and T. Huang, "Magic ring: A finger-worn device for multiple appliances control using static finger gestures," *Sensors*, vol. 12, no. 5, pp. 5775–5790, 2012.

[72] Y.-L. Hsu, C.-L. Chu, Y.-J. Tsai, and J.-S. Wang, "An inertial pen with dynamic time warping recognizer for handwriting and gesture recognition," *IEEE Sensors Journal*, vol. 15, no. 1, pp. 154–163, 2014.

[73] X. Gu, Y. Zhang, W. Sun, Y. Bian, D. Zhou, and P. O. Kristensson, "Dexmo: An inexpensive and lightweight mechanical exoskeleton for motion capture and force feedback in vr," in *Proceedings of the 2016 CHI Conference on Human Factors in Computing Systems*. ACM, 2016, pp. 1991–1995.

[74] J. F. O'Brien, R. E. Bodenheimer Jr, G. J. Brostow, and J. K. Hodgins, "Automatic joint parameter estimation from magnetic motion capture data," Georgia Institute of Technology, Tech. Rep., 1999.

[75] S. Yabukami, H. Kikuchi, M. Yamaguchi, K. Arai, K. Takahashi, A. Itagaki, and N. Wako, "Motion capture system of magnetic markers using three-axial magnetic field sensor," *IEEE transactions on magnetics*, vol. 36, no. 5, pp. 3646–3648, 2000.

[76] D. Vlasic, R. Adelsberger, G. Vannucci, J. Barnwell, M. Gross, W. Matusik, and J. Popović, "Practical motion capture in everyday surroundings," in *ACM transactions on graphics (TOG)*, vol. 26, no. 3. Acm, 2007, p. 35.

[77] T. B. Moeslund and E. Granum, "A survey of computer vision-based human motion capture," *Computer vision and image understanding*, vol. 81, no. 3, pp. 231–268, 2001.

[78] P. Merriaux, Y. Dupuis, R. Boutteau, P. Vasseur, and X. Savatier, "A study of vicon system positioning performance," *Sensors*, vol. 17, no. 7, p. 1591, 2017.

[79] B. Fang, F. Sun, H. Liu, and D. Guo, "Development of a wearable device for motion capturing based on magnetic and inertial measurement units," *Scientific Programming*, vol. 2017, 2017.

[80] A. Szczęsna, P. Skurowski, E. Lach, P. Pruszowski, D. Pęszor, M. Paszkuta, J. Słupik, K. Lebek, M. Janiak, A. Polański *et al.*, "Inertial motion capture costume design study," *Sensors*, vol. 17, no. 3, p. 612, 2017.

[81] P.-z. Chen, J. Li, M. Luo, and N.-h. Zhu, "Real-time human motion capture driven by a wireless sensor network," *International Journal of Computer Games Technology*, vol. 2015, p. 4, 2015.

[82] M. Paulich, M. Schepers, N. Rudigkeit, and G. Bellusci, "Xsens mtw awinda: Miniature wireless inertial-magnetic motion tracker for highly accurate 3d kinematic applications," *Xsens: Enschede, The Netherlands*, 2018.

[83] A. Filippeschi, N. Schmitz, M. Miezal, G. Bleser, E. Ruffaldi, and D. Stricker, "Survey of motion tracking methods based on inertial sensors: A focus on upper limb human motion," *Sensors*, vol. 17, no. 6, p. 1257, 2017.

[84] D. W. Allan, “Statistics of atomic frequency standards,” *Proceedings of the IEEE*, vol. 54, no. 2, pp. 221–230, 1966.